# On the Interface of Enzyme and Spatial Confinement: The Impacts of Confinement Rigidity, Shape, and Surface Properties on the Interplay of Enzyme Structure, Dynamics, and Function

Qiaobin Li,<sup>#</sup> Zoe Armstrong,<sup>#</sup> Austin MacRae,<sup>#</sup> Mary Lenertz,<sup>#</sup> Li Feng, and Zhongyu Yang\*

Department of Chemistry and Biochemistry, North Dakota State University, Fargo, ND, 58102

Corresponding to: <a href="mailto:zhongyu.yang@ndsu.edu">zhongyu.yang@ndsu.edu</a>

# These authors contribute equally to this work.

#### TABLE OF CONTENTS

#### I. INTRODUCTION

#### II. PRINCIPLES OF INVOLVED EPR METHODS

- 2.1. Continuous wave (CW) EPR to reveal backbone motion.
- 2.2. Revealing enzyme contact sites on confinement surface.
- 2.3. Probing spin exchange interactions among confined enzymes.
- 2.4. Probing protein clustering, oligomerization, and aggregations using CW EPR.
- 2.5. Pulsed EPR methods.
- III. ENZYME CONFINEMENT UNDER RIGID COMPARTMENTS WITH REGULAR SHAPES BASED ON METAL-ORGANIC FRAMWORKS (MOFS), COVALENT-ORGANIC FRAMEWORKS (COFS), AND MESOPOROUS NANOPARTICLES
  - 3.1. Effects of COF wall properties on enzyme catalytic efficiency.
  - 3.2. Enzyme structural basis within mesoporous silica-nanoparticles.
  - 3.3. Translocation of enzymes in MOF chambers.
- IV. ENZYME CONFINEMENT UNDER RIGID COMPARTMENTS WITH IRREGULAR SHAPES BASED ON CRYSTAL DEFECTS
  - 4.1. Classic co-crystallization to immobilize enzymes.
  - 4.2. Advanced co-crystallization platforms to provide advanced functionalities.
- V. POLYPEPTIDE CONFINEMENT UNDER FLEXIBLE, DYNAMICS CONFINEMENT BASED ON POLYMERIC MATERIALS

- 5.1. Polypeptides as probes to sense polymeric micelle interior environments.
- 5.2. Polypeptide dynamics and aggregation upon confinement in advanced micellar materials.
- 5.3. Polymer shells conjugated to enzyme surfaces.

# VI. CONCLUDING REMARKS AND OUTLOOK

#### Abstract

Confining proteins in synthetic nanoscale spatial compartments has offered a cell-free avenue to understand enzyme structure-function relationships and complex cellular processes near the physiological conditions, an important branch of fundamental protein biophysics studies. Enzyme confinement has also provided advancement in biocatalysis by offering enhanced enzyme reusability, cost-efficiency, and substrate selectivity in certain cases for research and industrial applications. However, the primary research efforts in this area have been focused on the development of novel confinement materials and investigating protein adsorption/interaction with various surfaces, leaving a fundamental knowledge gap, namely the lack of understanding of the confined enzymes (note that enzyme adsorption to or interactions with surfaces differs from enzyme confinement as the latter offers an enhanced extent of restriction to enzyme movement and/or conformational flexibility). In particular, there is limited understanding of enzymes' structure, dynamics, translocation (into biological pores), folding, and aggregation in extreme cases upon confinement, and how confinement properties such as the size, shape, and rigidity affect these details. The first barrier to bridge this gap is the difficulty in "penetrating" the "shielding" of the confinement walls experimentally; confinement could also lead to high heterogeneity and dynamics in the entrapped enzymes, challenging most protein-probing experimental techniques. The complexity is raised by the variety in the possible confinement environments that enzymes may encounter in nature or on lab benches, which can be categorized to rigid confinement with regular shapes, rigid restriction without regular shapes, and flexible/dynamic confinement which also introduces crowding effects. Thus, to bridge such a knowledge gap, it is critical to combine advanced materials and cutting-edge techniques to recreate the various confinement conditions and understand enzymes therein. We have spearheaded in this challenging area by creating various confinement conditions to restrict enzymes while exploring experimental techniques to understand enzyme behaviors upon confinement at the molecular/residue level. This review is to summarize our key findings on the molecular level details of enzymes confined in i) rigid compartments with regular shapes based on pre-formed, mesoporous nanoparticles and Metal-Organic Frameworks/Covalent-Organic Frameworks (MOFs/COFs), ii) rigid confinement with irregular crystal defects with shapes close to the outline of the confined enzymes via co-crystallization of enzymes with certain metal ions and ligands in the aqueous phase (biomineralization), and *iii*) flexible, dynamic confinement created by proteinfriendly polymeric materials and assemblies. Under each case, we will focus our discussion on a) the way to load enzymes into the confined spaces, b) the structural basis of the function and behavior of enzymes within each compartment environments, and c) technical advances of our methodology to probe the needed structural information. The purposes are to depict the chemical physics details of enzymes at the challenging interface of natural molecules and synthetic compartment materials, guide the selection of enzyme confinement platforms for various applications, and generate excitement in the community on combining cutting-edge technologies and synthetic materials to better understand enzyme performance in biophysics, biocatalysis, and biomedical applications.

#### **NOMENCLATURE**

Metal-Organic Framework: MOF

Covalent-Organic Framework: COF

Site-directed spin labeling: SDSL

Electron paramagnetic resonance: EPR

Continuous wave EPR: CW EPR

Double electron-electron resonance: DEER

Double quantum coherence: DQC

Microscopic order macroscopic disorder: MOMD

Non-linear least squares: NSLS

Zeolitic imidazolate framework: ZIF

Invertible micellar assembly: IMA

Polyethylene glycol: PEG

Polycaprolactone: PCL

Tetrahydrofuran: THF

#### I. INTRODUCTION

Enzymes are key biological catalysts essential to many cellular processes and thus, one of the central focuses of biophysics and biochemistry research. Enzymes have also been isolated from nature to serve as biocatalysts in materials, food, and biomedical research and industry. The high selectivity, specificity, and biocompatibility make enzymes ideal candidates to catalyze many reactions. 1-3 The drawbacks, however, are their relatively low stability once solubilized in buffer solutions over long-term storage (ca. months) at room temperature and high cost, which may be mitigated by immobilizing enzymes on solid surfaces and/or confining enzymes in nanoscale chambers. 4-10 Enzyme adsorption on or interaction with surfaces differs from enzyme confinement as the latter offers an enhanced extent of restriction to enzyme movement and/or conformational flexibility. Prior to our efforts, membrane protein unfolding upon interaction with surfaces 11-15 and protein orientation upon adsorption to charged surfaces have been investigated in the literature. 12, <sup>16-19</sup> Of particular interest to our team is enzyme confinement in porous materials, which not only offers enhanced enzyme stability and protection to allow for multiple catalytic cycles and/or as delivery platforms, but also provides substrate selectivity in certain cases.<sup>20-24</sup> Furthermore, confining enzyme in nanoscale chambers offers an avenue to mimic the confined cellular environment that enzymes experience in nature, which may avoid the complexities caused by the cellular components. By doing so, cell-free enzyme biophysics studies such as how confinement affects enzyme structure, dynamics, function, transport (into biological pores), misfolding, and aggregation under certain scenarios can be carried out in a convenient way.

Thus far, the majority of research efforts in enzyme confinement studies has been focused on developing novel materials to mimic cellular compartments and/or achieve desired catalytic performance.<sup>5, 8, 25-33</sup> In spite of the large, vivid collection of confinement materials and methods

developed to date, there is a fundamental knowledge gap on the behavior of the confined enzymes at the molecular level. In particular, how enzymes adjust their structure and conformational dynamics to fit to the confined space, how enzyme function is affected by the confinement, and how confinement properties such as size, shape, and rigidity impact answers to the former two questions remain unanswered. Lacking answers to these questions prevents the rational design of confinement platforms for the custom immobilization of enzymes with desired structure, dynamics, and function as well as for more effective mimicking of the cellular confinement conditions.

Filling in this gap is a challenging task. It not only requires the proper ways to tune confinement properties/factors but also specific experimental techniques to probe the needed structural and dynamic information through the shielding of the confinement walls. Furthermore, the performance of the same enzyme under varied confinement conditions needs to be compared in order to reveal how confinement conditions impact enzymes. Upon a careful examination of the complex enzyme confinement cases in nature and on lab benches, we found that the typical chambers can be categorized to 3 major cases, rigid chambers with shapes independent of enzyme, rigid chambers with shapes resembling the outlines of target enzymes, and soft chambers "wrapping" the target enzymes, the latter of which also involves crowding effects. In the past 5-6 years our group developed a set of tools/procedures to probe biomacromolecules under all three confinement conditions and applied these methods to study various enzymes, including T4L at the molecular level based on site-directed spin labeling (SDSL) in combination with electron paramagnetic resonance (EPR) spectroscopy. 34-53 SDSL-EPR offers a unique avenue to probe the structural and dynamical information of a labeled enzyme in complex biological or artificial environment regardless of the heterogeneity and "shielding", perfect for probing enzymes under various confinement conditions. A unique opportunity of exploring various confinement materials

is to compare enzyme performance and the underlying structural basis of the same enzyme, which offers a unique opportunity to reveal how confinement size, shape, and rigidity impact enzyme biophysics.

This review is to provide an up-to-date summary of our key findings on the molecular level structural and dynamic basis of enzymes confined in i) rigid compartments with regular shapes based on pre-formed, mesoporous nanoparticles and Metal-Organic Frameworks/Covalent-Organic Frameworks (MOFs/COFs), ii) rigid confinement with irregular shapes (likely the outline of the confined enzymes) based on co-crystallization of enzymes with certain metal ions and organic ligands in the aqueous phase (biomineralization), and iii) flexible, dynamic confinement created by polymeric materials and assemblies. Under each case, we will discuss a) the way to load enzymes into the confined spaces, b) the dynamics and contact sites of the enzymes within each compartment environments, and c) technical advances of our methodology to probe the needed structural information. Lastly, we complete this review by comparing the structure and dynamics information of the same enzyme upon confinement in different chambers. The purposes are to report the chemical physics details of enzymes at the challenging interface of natural molecules and synthetic materials, guide the selection of enzyme confinement platforms for various applications, and generate excitement in the community on combining cutting-edge technologies and synthetic materials to better understand enzyme performance in biophysics, biocatalysis, and biomedical applications. There have been reviews on each of the three ways to confine enzymes in the literature. However, this work overviews the three different ways to confine enzymes and reviews the impact of different confinement platforms on (the same) enzymes. Furthermore, this work is focused on correlating the structural basis of enzymes with their catalytic performances under confinement. The general applications of EPR on enzyme studies can be found in review articles well-documented in the literature which will not be discussed in detail here.<sup>35, 54-58</sup>

#### II. PRINCIPLES OF INVOLVED EPR METHODS.

#### 2.1. Continuous wave (CW) EPR to reveal backbone motion.

CW EPR is a classic biophysics experimental technique to probe paramagnetic electron spin centers such as radicals and paramagnetic metals. The physical principles have been well-documented in textbooks and thus, will not be repeated here. In biological especially protein science applications, EPR is often combined with spin labeling as most proteins are diamagnetic and thus, EPR-silent. The most popular labeling strategy is covalently linking a nitroxide radical to a protein cysteine through a disulfide bond, generating a sidechain often named as R1 (Figure 1A). 55, 59-65 The small label size (close to a sidechain; Figure 1B) and the relatively low abundance of cysteine in nature make this approach applicable to most proteins (cysteine-rich proteins can be labeled via unnatural amino acids). 66 The EPR signal of a labeled protein depends on three motions, protein rotational tumbling, protein backbone fluctuation, and the intrinsic motion of the spin label sidechain (Figure 1B), as well as the available space for the sidechain to move around (ordering). 39,

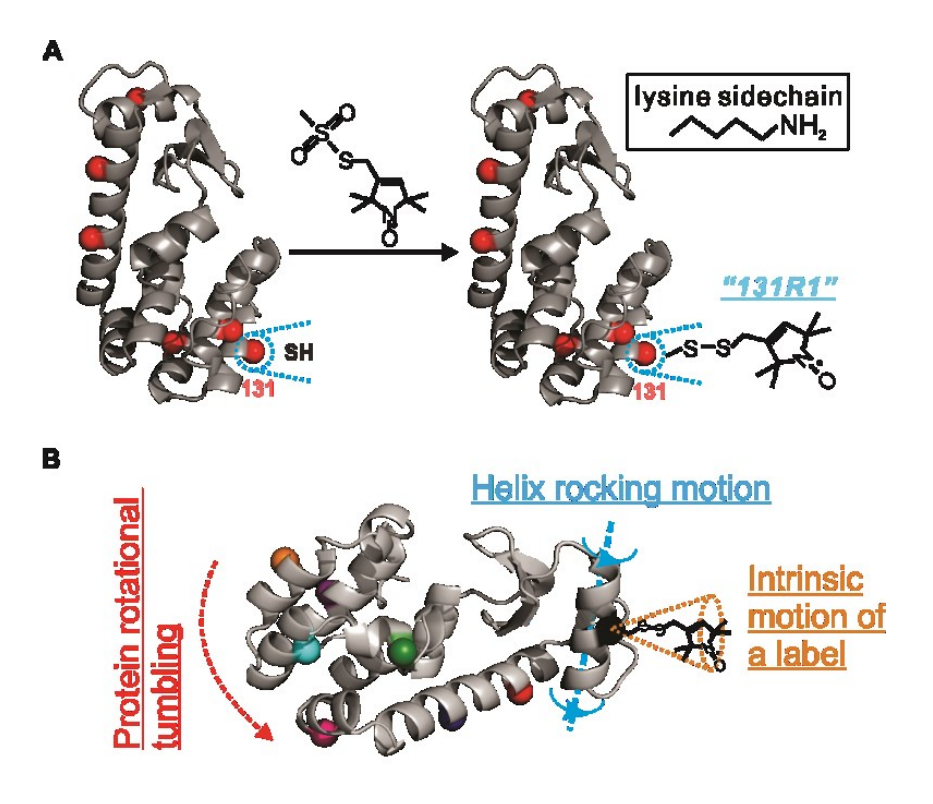


**Figure 1.** (A) SDSL of a protein residue to generate a labeled sidechain (blue). (inset) the size of a lysine sidechain which is comparable to a R1 sidechain generated by SDSL. (B) Three types of rotational motions that could affect the CW EPR signal when a spin label is attached to a protein via SDSL.

The total rate is dependent on the three motions via:

$$\frac{1}{\tau_{tot}} = \frac{1}{\tau_{protein}} + \frac{1}{\tau_{backbone}} + \frac{1}{\tau_{SL}}$$
 Equation 1

where  $\tau_{tot}$  represents the total correlation time, while  $\tau_{protein}$ ,  $\tau_{backbone}$ , and  $\tau_{SL}$  are the correlation times of protein rotational tumbling, protein backbone fluctuation, and the intrinsic motion of the spin label sidechain, respectively.<sup>67</sup> These factors depend on protein states. For example, a small free protein (<45 kDa) in solution will show a relatively sharp EPR spectrum (Figure 2A; 3 lines

are due to the electron-nuclear spin hyperfine interactions; CW EPR usually reports first-derivative spectra) due to an averaging of all three types of motions. An unfolded protein will show a sharper spectrum due to the enhanced backbone motion (typically <0.5 G linewidth; Figure 2B). A protein attached to a solid support (or restricted in a confined chamber), on the other hand, will lead to restriction in rotational tumbling and thus, a broader spectrum (Figure 2C). Typical spectral lineshapes of these relatively fast motions often fall into the spectral areas highlighted by "m" in Figure 2 (often named as the "mobile" or "m" spectral component). If the labeled sidechain is in contact with a solid surface upon being trapped in a chamber, then all three motions are limited, resulting in an extremely broad spectrum (Figure 2D). Typical spectral lineshapes of this relatively restricted motion often fall into the spectral areas highlighted by "im" in Figure 2 (often named as the "immobile" or "im" spectral component). If multiple cases are present in the same system, then CW EPR will show a multi-component spectrum (Figure 2E), deconvolution of which through spectral simulations can resolve the contribution/population of different components together with the associated motional and ordering parameter. These can be analyzed further to reveal enzyme contact sites and motion upon confinement. The key of using CW EPR to probe enzymes, thus, lies on spectral simulation.

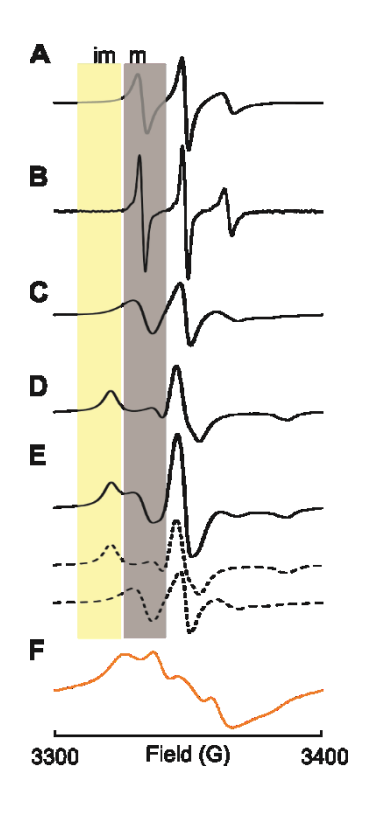
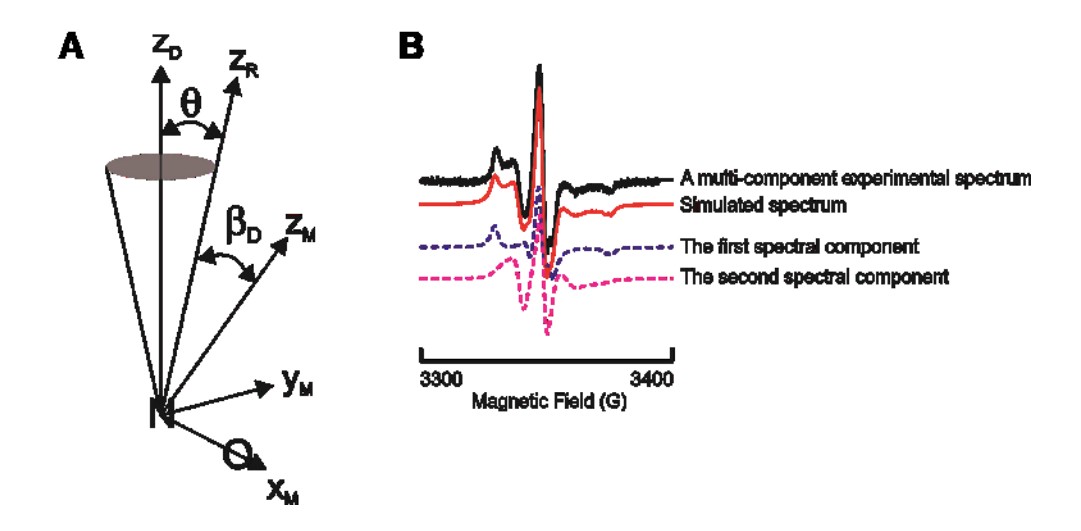


Figure 2. Examples of typical CW EPR spectra for various cases at room temperature: a free protein in solution (A), an unfolded protein (B), an immobilized protein (C), an immobilized protein while contact a solid surface with the labeled site (D), a heterogeneous case with spectral deconvolution (E), and a typical Pake Pattern when short inter-spin distances are present (F). The areas highlighted by "m" and "im" are originated from a spin labeled sidechain with relatively mobile and immobile motions, respectively. The scale of all EPR spectra is 3300 to 3400 G.

The physics of the fitting program is based on the microscopic order macroscopic disorder (MOMD) model of the non-linear least squares (NSLS) program established by Freed and coworkers, <sup>68</sup> which has various user interfaces such as Multicomponent developed by Altenbach and Hubbell (<a href="http://www.biochemistry.ucla.edu/biochem/Faculty/Hubbell/">http://www.biochemistry.ucla.edu/biochem/Faculty/Hubbell/</a>) and EasySpin by Stoll. <sup>69</sup> In protein studies, the MOMD model employs three coordinate frames to describe the internal

motion of a nitroxide spin label in an enzyme. First, the molecular frame is consistent with the magnetic tensor (g- and hyperfine-tensor) frame ( $x_M$ ,  $y_M$ ,  $z_M$ ). The  $z_M$  is defined as to be along with the nitroxide  $p_z$  orbital; the  $x_M$  is parallel with the NO bond axis; the  $y_M$  follows a right-handed coordinate system. Second, the principle frame of the rotational diffusion tensor ( $x_R$ ,  $y_R$ ,  $z_R$ ) usually deviates from the molecular frame. Three Euler angles are required to correlate the two frames, which affect the results of the simulation of the spectrum ( $\alpha_D$ ,  $\beta_D$ ,  $\gamma_D$ ). Third, the coordinate frame describes the diffusion of the spin label on the attached enzyme, the director frame ( $x_D$ ,  $y_D$ ,  $z_D$ ). A good approximation/simplification is to allow the spin label to rotate/move freely within a cone (Figure 3A). This also leads to simplifying the rotational diffusion tensor R wherein the axial symmetry can be assumed. The angle between  $z_D$  and  $z_R$  is defined as  $\theta$  (Figure 3A).



**Figure 3.** (A) Definition of coordination systems in a MOMD model. (B) An example spectral simulation (red solid) using the MOMD model to fit a typical multi-component EPR spectrum (black solid). The two spectral components can be deconvoluted into two spectra (dotted black and red curves). Reprinted (adapted) with permission from ACS Appl. Mater. Interfaces 15, 38124 (2023). Copyright 2023 American Chemical Society.

According to Budil et al,<sup>68</sup> a restoring (ordering) potential (*U*) is appropriate to describe the extent of spatial constraints of the spin label within the "cone" (Figure 3A). The restoring potential is  $U(\theta) = -1/2k_BTc_0^2$  ( $3\cos^2\theta - 1$ ) + H.O.T., where  $c_0^2$  is a scaling coefficient and H.O.T. represents higher order terms as defined in the literature.<sup>68</sup> The ordering parameter often utilized in simulations, S, is defined as S=1/2(3<cos<sup>2</sup> $\theta$ >-1), where  $\theta$  is defined in Figure 3A and the triangle- brackets indicate spatial average.<sup>68</sup> In most simulations, only the dominant term and the first H.O.T. term are involved, the coefficients of which are  $C_{2\theta}$  and  $C_{22}$ , respectively.

We found the following procedures work well with enzymes under confinement using synthetic materials. The starting values for the diagonal values of the g and hyperfine (A) tensors were:  $g_{xx} = 2.0078$ ,  $g_{yy} = 2.0058$ ,  $g_{zz} = 2.0022$  and  $A_{xx} = 6.2$  G,  $A_{yy} = 5.9$  G,  $A_{zz} =$  between 34.5 and 36.5 G.71 The hyperfine parameter, Azz, reflects the local hydrophobicity. In hydrophobic environments, Azz is usually 34.5-35.0 G, while it becomes 35.0-37.5 G under hydrophilic conditions. The rotational correlation rates are described by the rotational diffusion tensor. For simplicity, symmetric motion is assumed and this assumption is found to provide reasonably good fit to the data. The mean rotational diffusion constant is defined as R. 68 The average effective correlation time is computed as  $\tau_c = 1/(6R)$ . Spatial ordering of the diffusion tensor is accounted for by the order parameters,  $S_{20}$  and  $S_{22}$ , computed from the  $C_{20}$  and  $C_{22}$  coefficients of the ordering potential which was varied in fitting.<sup>68</sup> The tilt of the diffusion tensor with respect to the molecular axis of the nitroxide is specified by the Euler angles  $(\alpha_D, \beta_D, \gamma_D)$ . For axially symmetric motion  $(R_x)$  $= R_{\nu}$ ), only  $\beta_D$  and  $\gamma_D$  need be specified. For z-axis anisotropic motion, the starting value of the diffusion tilt is  $\beta_D = 36^{\circ}$  which can be changed during simulations.<sup>72</sup> An additional rotational diffusion constant,  $R_2$ , is defined as  $R_z$ - $(R_x$ - $R_y)/2$ . This term is defined to describe the anisotropy in the motion of the spin label in the x-, y- and z-axes/directions. This term, together with  $R_I$  which is defined as the average rate of the motion of the spin label in the x-, y- and z-axes/directions  $(R_I=I/3(R_x+R_y+R_z))$ , are utilized in simulation to quantify the spectral contribution from motion.<sup>68</sup>

The R,  $C_{20}$ , and  $C_{22}$  parameters are varied in the simulations to fit the experimental data. After a good fit was obtained, the diagonal elements of the A and g tensors can be varied slightly to obtain the best fit. Using these procedures, CW EPR spectra of spin labeled enzymes confined in various chambers can be simulated, resulting in key rate and order parameters (typical spectral simulation see Figure 3B).

### 2.2. Revealing enzyme contact sites on confinement surface.

Experimentally, revealing biomacromolecules' contact sites on a solid surface is a non-trivial task as it requires detecting the areas or regions of the biomacromolecule contacting the surface at the sub-molecular level resolution (ideally residue level resolution). EPR and spin labeling offer a unique and rapid opportunity to achieve this goal. The principle is that, upon contact with a solid surface, a protein/enzyme's contact with the surface via a labeled residue will result in enhanced restriction in the motion of the residue's sidechain and thus, reduced rate (*R*) and enhanced ordering (*S*) parameters, both of which could be quantified via EPR spectral simulation. Scanning representative surface regions of a target enzyme will therefore lead to protein regions responsible for contact (Figure 4 red spectrum); the protein contact sites are likely "sitting" on the surface via these contact regions while pointing the rest regions away from the surface. This strategy is suitable for both flat and concave surfaces (such as a protein inside a confined chamber; Figure 4A).<sup>39</sup> It is also possible to reveal protein regional freedom if the protein is partially buried in a solid scaffold (Figure 4B). If the contact sites are heterogeneous, then EPR spectral analysis can report the relative chance for a region to contact the solid surface by

determining the relative population of the "contact" component, which shows more restricted motion in comparison to that with relatively high mobility (Figure 4 red vs green spectra). Such multi-component spectral simulation can reveal up to 3 different categories of motions, sufficient for probing enzyme contact sites as proved in our recent works discussed in below sections.<sup>39</sup>

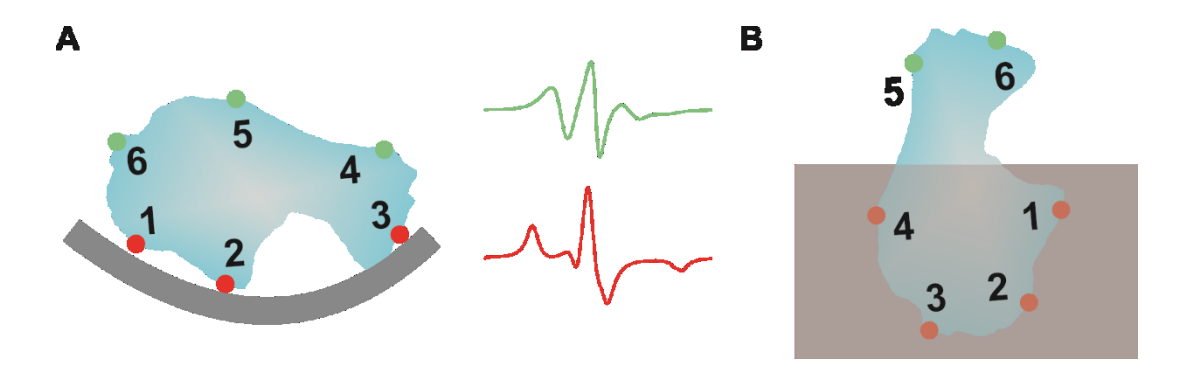


**Figure 4.** Illustration of the strategy to use CW EPR to determine enzyme contact sites on a solid surface (A) or upon being buried under a porous scaffold (B). Protein regions under contact with a solid support usually shows a highly restricted motion (typical spectrum shown in red) as compared to those hanging in space (green). EPR spectral range is 3300 to 3400 G. Both representative spectra are taken under room temperature.

# 2.3. Probing spin exchange interactions among confined enzymes.

Depending on confinement wall properties, it may be possible to observe a highly symmetric central peak and a highly reduced low-/high-field peak.<sup>73-75</sup> The resultant spectra cannot be fit with the MOMD model as detailed in 2.1. This characteristic spectrum is caused by spin exchange interactions. In general, when two spin centers are close to each other (ca. <10 Å), spin exchange can occur.<sup>76, 77</sup> Due to the intrinsic size of enzymes, upon confinement in a chamber, it is unlikely for two labeled sidechains to be closer than the size of the protein (typically a few nm).

Thus, under normal conditions (no confinement), spin exchange usually indicates protein misfolding/aggregation or the aggregation of disordered polypeptide. Under spatial confinement in compartments with walls which promote conductivity or contain conjugated  $\pi$  structures such as aromatic rings, it is also possible for spin exchange to occur, because if a the spin labeled sidechain contacts strongly with the confinement walls, the electron in the radical sidechain can hop onto the wall and travel along the wall to be exchanged with other electrons from nearby labeled enzymes.<sup>46</sup> Thus, in combination with SDSL, probing spin exchange offers an opportunity to determine which residues of an enzyme that can contact strongly with the confinement walls.

The impact of spin exchange on the lineshape of CW EPR spectra (a symmetric central peak and a reduced low-/high-field peak) could be reflected by some empirical parameters which could be derived depending on the target system.<sup>78, 79</sup> Based on our experience in enzyme EPR under confinement, wherein a highly immobilized, broadened spectrum (example see Figure 5) is observed in the absence of spin exchange,<sup>46</sup> we derived two empirical parameters based on the ratio of the positive and negative peak heights of the central peak, namely  $I_{cp}/I_{cn}$ , and the height ratio of the low-field peak to the central peak, namely  $I_{0}/(I_{cp} + I_{cn})$  (peak definitions see Figure 5).<sup>46</sup> The closer the  $I_{cp}/I_{cn}$  to 1, the more symmetric the central peak, and the stronger the spin exchange interactions. Typical value of 1.5-1.6 indicates minimal exchange while  $I_{cp}/I_{cn}$  of <1.4 suggests the presence of exchange.<sup>46</sup> Furthermore, the smaller the  $I_{0}/(I_{cp} + I_{cn})$ , the more reduced low-field peak, and the stronger the spin exchange interaction, the stronger the enzyme contact with the wall via the labeled site. These parameters, however, are only to give the relative strength of spin exchange, instead of an absolute strength.

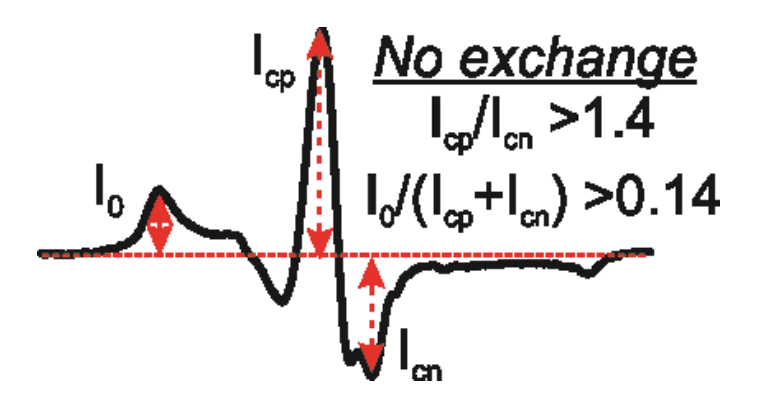


**Figure 5.** Basic criteria of using CW EPR lineshape to determine the relatively strength of spin exchange interactions in a CW EPR spectrum from a typically immobilized labeled site. Typical scan range is 3300 to 3400 G.

### 2.4. Probing protein clustering, oligomerization, and aggregations using CW EPR.

If two spin labeled sidechains are separated by 10-25 Å, the magnetic dipolar interaction between the two can lead to CW EPR spectral broadening (Figure 2F). The resultant spectra cannot be fit with the MOMD model as detailed in 2.1 because the dipolar interaction terms are not included in the MOMD model. Instead, a separate procedure, quantifying the broadening caused by the presence of nearby spin centers, has been developed to determine distances between adjacent spin labels. The broadening is termed as the Pake Pattern (Figure 2F), which can be simulated using the ShortDistance program (<a href="https://sites.google.com/site/altenbach/labview-programs/epr-programs/short-distances?authuser=0">https://sites.google.com/site/altenbach/labview-programs/epr-programs/short-distances?authuser=0</a>) developed by Altenbach and Hubbell. 80-85 For enzymes under confinement, this approach can be used to determine the distances between adjacent proteins/polypeptides (singly labeled) and thus, oligomerization of the labeled proteins/polypeptides. This information is important for assessing if confinement induces protein aggregation and thus, critical for protein hosting and delivery applications.

#### 2.5. Pulsed EPR methods.

Various pulsed EPR methods have also been developed to probe enzyme biophysics. In comparison to the CW EPR methods, these pulsed EPR methods offer longer range of inter-spin label distances and distance distributions in enzymes (2-7 nm), slower dynamics of enzyme backbone motion (up to tens of µs), and other critical information (such as water accessibility, coordination of the spin center, etc). Since our group has not extensively explored pulsed EPR in our enzyme-confinement studies, in this review, we will not discuss the principles of these pulsed EPR techniques. Interested readers are referred to a few excellent reviews. <sup>54, 86-88</sup>

III. ENZYME CONFINEMENT UNDER RIGID COMPARTMENTS WITH REGULAR SHAPES BASED ON METAL-ORGANIC FRAMEWORKS (MOFS), COVALENT-ORGANIC FRAMEWORKS (COFS), AND MESOPOROUS NANOPARTICLES.

# 3.1. Effects of COF wall property on enzyme catalytic efficiency.

COFs are rigid, tunnel like porous materials with a few nm diameter and µm lengths. Most COFs maintain hexagonal shapes although other shapes have also been developed. 89, 90 Enzymes smaller than COF pores can be loaded into certain COF channels via diffusion over the timescale of hours to days, which often offers enhanced enzyme stability and substrate selectivity. 91, 92 Revealing the structure-function relationship of the confined enzymes, however, is challenging, due to the interference of the COF walls with most protein-probing techniques. We recently demonstrated the use of SDSL in combination with EPR spectroscopy to probe the structure-function relationship of a model enzyme, T4 phage lysozyme (T4L) in various MOFs/COFs. 46 We also modified the functional groups of the COF inner walls to adjust the hydrophobicity and revealed the impact of wall hydrophobicity on the interplay of protein structure, function, and dynamics.

In detail, we modified the -OMe groups of a COF to -OH and -ONa, forming 3 COFs, COF-OMe, COF-OH, and COF-ONa with decreasing hydrophobicity but identical diameter (3.4 nm; Figure 6A). 92 We then loaded T4L into each COF as demonstrated by confocal fluorescence imaging and porosity test. 46 To probe the catalytic performance of T4L, we employed a small substrate of T4L, 11-chitosan which can diffuse into the COF channels and interact with T4L. In the presence of free T4L, the activity assay detailed in the literature generates a decrease in the absorption intensity at 420 nm as compared to no enzyme (a 0.81 to 0.25 arbitrary unit (a.u.) drop; Figure 6B pink versus black dotted curves; Table 1).46 T4L loaded in COF-OMe showed a drop from 0.81 to 0.29 a.u. (Figure 6B red solid versus black dotted curves; Table 1), ~92.9 % of the catalytic efficiency of free T4L. T4L loaded in COF-OH showed a drop from 0.81 to 0.55 a.u. (Figure 6B green solid *versus* black dotted curves; Table 1), ~46.4 % of the catalytic efficiency of free T4L. T4L loaded in COF-ONa showed almost no change in the absorption at 420 nm (Figure 6B purple solid versus black dotted curves; Table 1). Thus, T4L possessed a decreased catalytic efficiency as the channel hydrophilicity was increased (from -OMe to ONa), unusual for a hydrophilic enzyme like T4L (Figure 6B).

Table 1. Quantitative measure of T4L activity in solution and upon encapsulation in COFs using the activity assay detailed in the literature.<sup>46</sup>

	No T4L	Free T4L	T4L@COF-	T4L@COF-OH	T4L@COF-
		(control)	OMe		ONa
Absorption at	0.81	0.25	0.29	0.55	0.80
420 nm (a.u.)					
Drop in		0.56	0.52	0.26	0.01
Absorption at					
420 nm (a.u.)					

To understand this, we employed SDSL to label 6 sites of T4L and probed backbone dynamics at the labeled regions in each COF. We found similar spectra among all six labeled sites

of T4L in COF-OMe, which can be explained by a portion of T4L contacting the channel walls at the labeled site while the rest hanging in COF-OMe channel chambers (Figure 6C left). Then, in COF-OH, we found 2 out of the 6 labeled sites displayed distorted CW EPR spectra as characterized by the reduced low-field peak and symmetric center peak (Figure 6C right). We rationalized this to the spin exchange interactions between an electron spin in a protein and another from adjacent proteins (also see Section 2.2): once a protein contacts the wall strongly via the labeled site, the electron hops onto the conjugated  $\pi$  tunnels and exchange with others. The highly conjugated  $\pi$  stacking system facilitates the tunneling of electrons. The fact that 2 sites of T4L interact strongly with the COF-OH channel suggests that at least two sites of T4L are strongly interacting with and thus, restricted by the COF-OH walls, leading to reduced conformational freedom and thus, reduced catalytic efficiency. Quantitatively, we defined  $I_{cp}/I_{cn}$  as a measure of exchange interactions so that  $I_{cp}/I_{cn}$  below 1.4 and/or  $I_0/(I_{cp}+I_{cn})$  <0.14 indicates strong interactions (Figure 6D).<sup>46</sup>

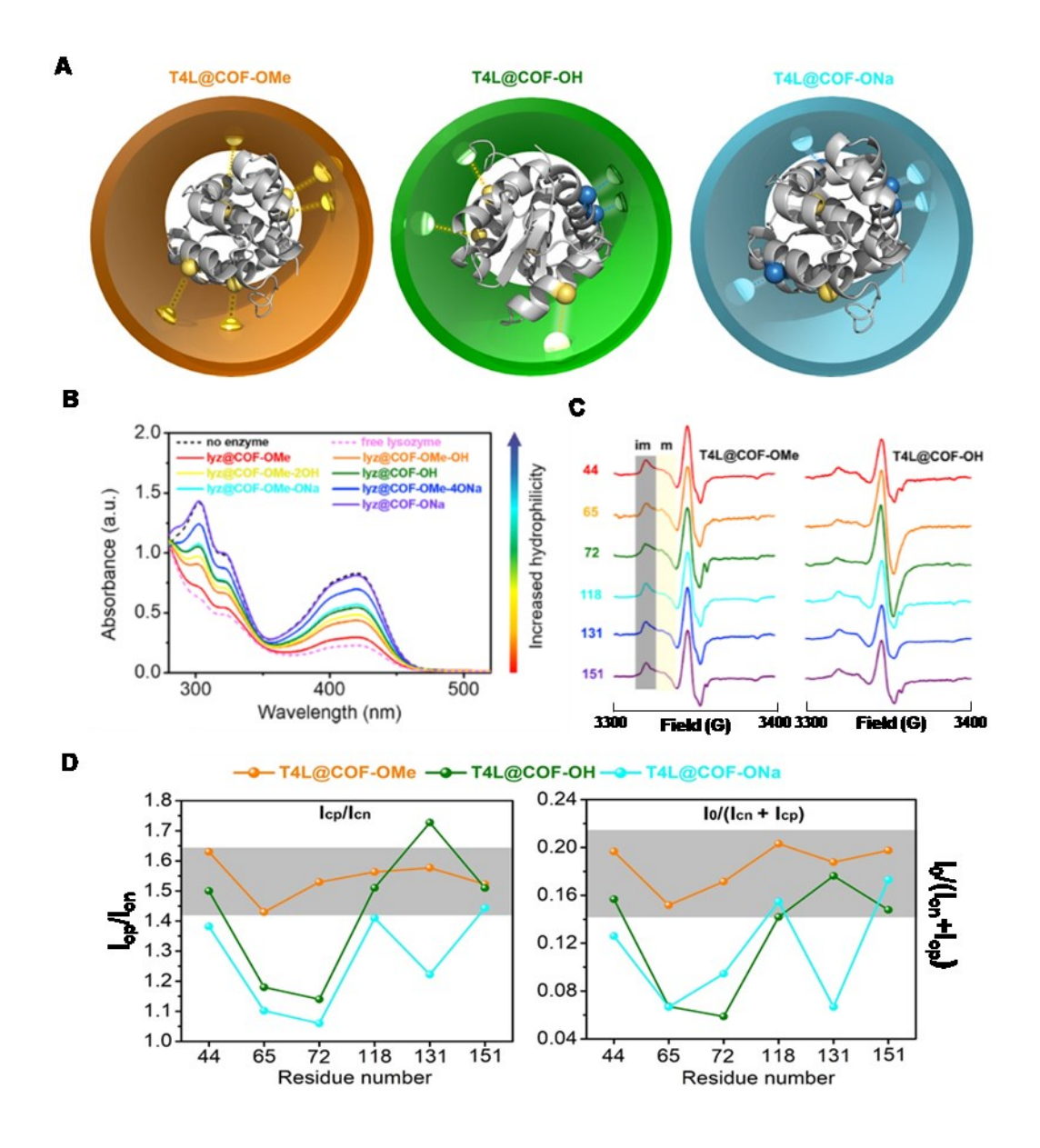


Figure 6. (A) Illustration of three COF channels with different surface properties. (B)

Differences in T4L catalytic efficiency upon immobilization in each COF. (C) Representative

CW EPR spectra of each labeled T4L in COF-OMe and COF-OH at room temperature. The

areas highlighted by "m" and "im" are originated from a spin labeled sidechain with relatively

mobile and immobile motions, respectively. The field scan range is 3300 G to 3400 G. (D) Plots

of key parameters related to spin exchange interactions as a function of labeled residue number.

Reprinted (adapted) with permission from Chem Catal. 1, 207 (2021). Copyright 2021 Elsevier.

Similarly, in COF-ONa, 4 out of the 6 labeled sites showed enhanced contact and reduced conformational freedom. Thus, as the channel became more hydrophilic, the number of T4L residues that strongly contact COF walls was increased, resulting in an enhanced restriction in T4L degree of freedom. Such restriction caused the reduced catalytic efficiency in the more hydrophilic COFs. This finding indicates the important role of spatial confinement in protein dynamics/function and the effectiveness of SDSL-EPR in probing the underlying structural basis of protein function alteration in nanoscale spatial confinement.

#### 3.2. Enzyme structural basis within mesoporous silica-nanoparticles.

Mesoporous silica-nanoparticles (mesoSiNPs) also contain rigid pores, although with lower homogeneity in pore size. We loaded spin labeled T4L into the pores of commercial mesoSiNPs. Upon removal of surface adsorption proteins via wash with a highly ionic buffer, CW EPR was carried out to detect the interaction of each labeled residue with the inner walls of the mesoSiNPs. A set of spectra characterized by a highly restricted component and a relatively mobile one was determined. Similar to Section 3.1, the restricted component is originated from label contacting the inner walls of the channels while the mobile one due to labeled site hanging in the chamber (Figure 7A). Upon EPR spectral simulation, parameters of the rate and order of each component of each labeled site were resolved.<sup>39, 40, 53</sup> We also found the relative contribution of the two cases for each labeled site (6 surface sites total), which led to the proposed protein contact sites inside of the mesoSiNP channels (Figure 7B). Interestingly, by tuning the surface charge of the channels, it is possible to alter the interaction between T4L and the channel, and thus, tune the encapsulation of the protein. Enzymes can be released under reducing conditions from these

mesoSiNPs, likely an advantage as compared to COFs, wherein the loaded enzyme cannot be easily released.<sup>53</sup>

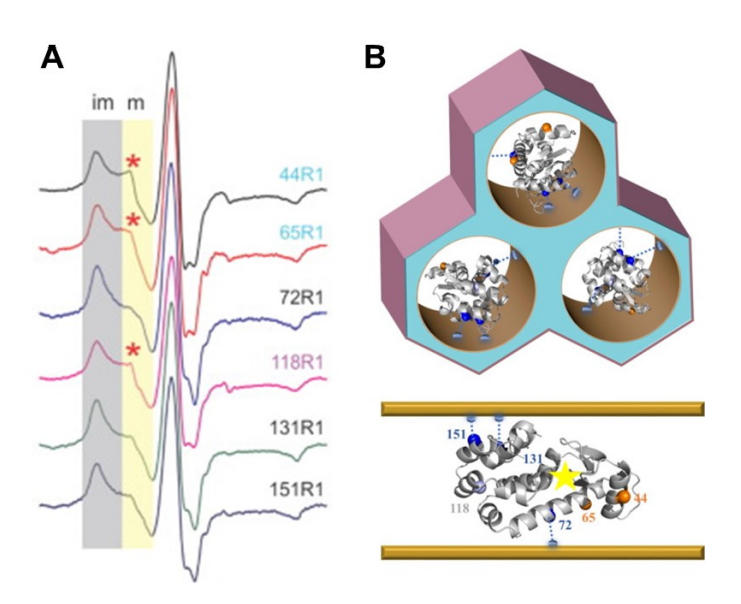


Figure 7. (A) CW EPR spectra at room temperature on six labeled sites of T4L. \* indicates spectral components that is originated from a label not in contact with the channel. The field scan range is 3300 G to 3400 G. (b) (upper panel) Illustration of the encapsulation of T4L in the channels of the mesoporous silicananoparticles. (lower panel) Illustration of the protein contact sites in the channels of the mesoporous Silica-nanoparticles. Dotted lines indicate relatively stronger interaction between the labeled residue and the channel. Star = lys active site. 53

Reprinted (adapted) with permission from J. Magn. Reson. Open 10-11, 100060 (2022).

Copyright 2022 Elsevier.

# 3.3. Translocation of enzymes into MOF chambers.

Although diffusion and enzyme-channel wall interactions are likely the driving forces of enzyme loading/transfer into rigid pores, the detailed structural basis of the transport, such as

changes in the contact sites and backbone dynamics of a protein during a transport event in real time and how channel properties affect protein transport, is generally lacking. However, such structural basis is important for understanding the causes of protein structural changes during a transport process in nature and predicting the resultant enzyme structure-function relationship. 93-<sup>97</sup> We employed time-resolved EPR and a series of chamber materials to initiate bridging this gap. In detail, we chose a COF with a larger pore (~4.5 nm) than COF-OMe, namely, COF-ETTA-TPDA, and time-resolved EPR to study the transfer of the same model enzyme, T4L, into it.<sup>37</sup> To probe the heterogeneity in protein-COF surface contact, we labeled 6 surface sites of T4L and triggered the transport of each spin labeled T4L (Figure 8A). Time-resolved CW EPR was then carried out to probe the change in backbone dynamics of various T4L regions during the transport. In particular, over time, the intensity of the mobile component (mobility of the spin label) was decreased as T4L was translocated into channels while that of the "contact" or relatively more immobile component was increased (definitions see Section 2.2; experimental data see reference).<sup>37</sup> The "contact" component was due to T4L interaction with channel walls at the labeled site. Note that other sources of immobilization such as protein aggregation could not contribute to the "contact" component. This may be caused by the relative narrow space in the channels, which may help prevent aggregation. More importantly, from EPR spectra, we did not observe any indication of aggregation (spin exchange or magnetic dipole-dipole interaction which would broaden the spectra).<sup>37</sup>

The spectral component caused by the contact with COF channels was then plotted for each labeled site over time. In general, a 2-phase transition was observed for most sites, a rapid initial adsorption to COF surfaces likely due to hydrophobic interactions (~10-30 minutes) and a slower move into the channels due to diffusion (up to 48 hours; Figure 8C&E).<sup>37</sup> Interestingly, different

labeled sites displayed different kinetics, so that 65 and 72 showed the least affinity to the COF surface, as indicated by the lowest percentage of contact component (Figure 8E). This was rationalized to the least population of aromatic residues in T4L near these regions (Figure 8G). The protein likely contacts the channel surface with other regions besides 65 and 72. The second phase of the transport is less residue dependent, suggesting the diffusion is a random process.

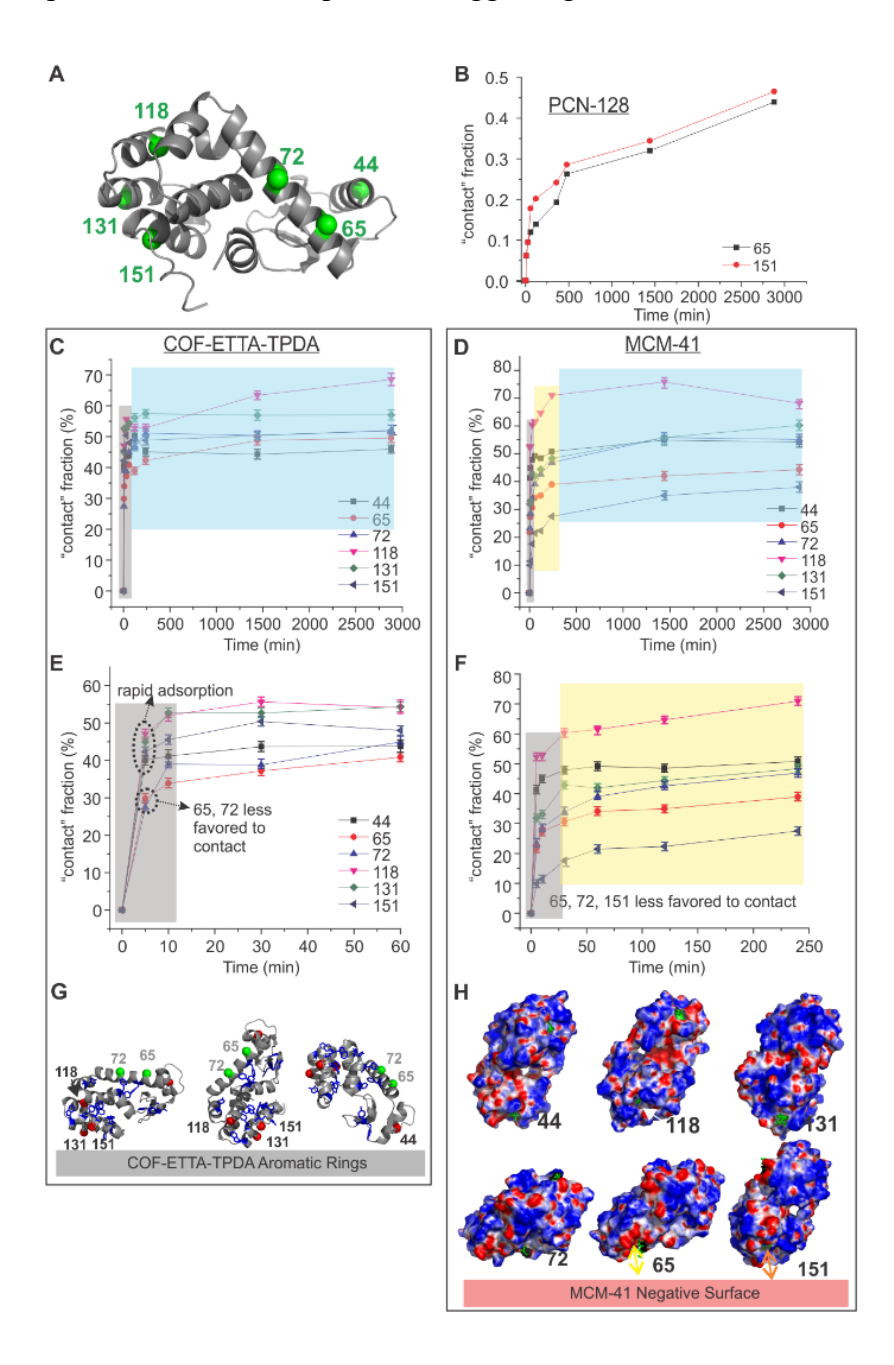
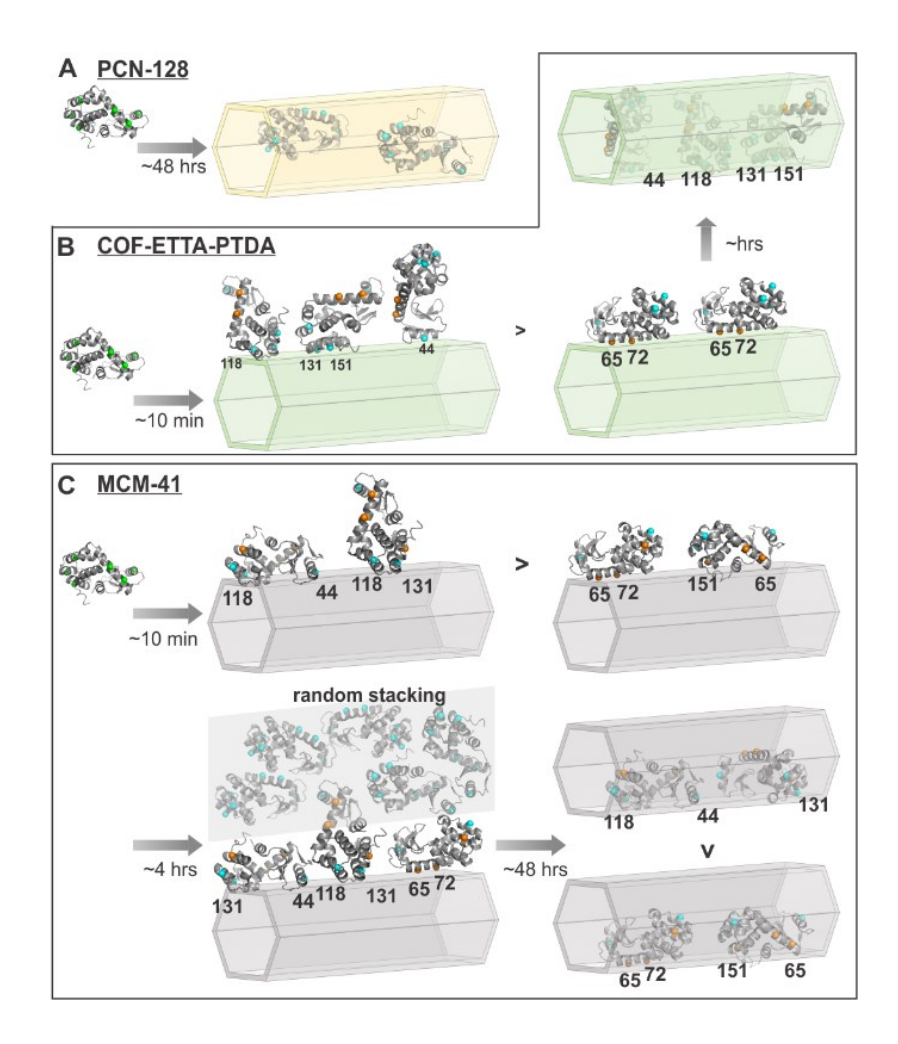


Figure 8. (A) Positions of labeled residues in T4L. The relative population of the "contact" spectral component of lys mutants upon translocation into PCN-128 (B), COF-ETTA-TPDA (C), and MCM-41 (D) was monitored for 48 h. Due to the lack of preference in contact sites, on PCN-128 only data from two sites are shown. The first hour is amplified to show the rapid adsorption in early times for COF-ETTA-TPDA (E) and MCM-41 (F). The distribution of aromatic residues (blue sticks) with respect to the labeled sites (G) and that of protein surface charge (H; blue=positive; red=negative) are shown to assist in data interpretation.

To probe the impact of channel property on protein transport, we chose 2 more channels with neutral and negatively charged surfaces (but the same pore size, ~4.5 nm), PCN-128 (a channel-shape MOF), and MCM-41 (mesoporous silica nanoparticles), respectively. <sup>21, 98, 99</sup> T4L labeled at various surface residues was employed to probe the impact of wall surface on its import into each channel. We found that the neutral, PCN-128 channels resulted in a single-phase process with a slow loading rate and random contact sites (which can be probed by detecting which residues/regions contact a channel), suggesting diffusion as the driving force (Figure 8B). No residue dependence was found either, suggesting the lack of preferential interaction between T4L and PCN-128 channels. <sup>37</sup> The negatively chargedMCM-41 channels, on the other hand, resulted in a 3-phase import, a rapid adsorption to MCM-41 surface, a "stacking" to form a multi-layer protein corona, <sup>19</sup> and finally a slower move into the channels (Figure 8D&F). <sup>37</sup> The contact sites of T4L with respect to MCM-41 surface were also found consistent with the surface charge distribution (Figure 8H). Based on these time-resolved data, we have proposed the dynamic process of the translocation of T4L into each channel (Figure 9). This work proved the

effectiveness of SDSL-EPR in probing protein-channel interactions during a transport event in real time.



**Figure 9.** The contact site changes of T4L at different phases of translocation into PCN-128 (A), COF-ETTA-TPDA (B), and MCM-41 (C). Cyan spheres indicate residues with a higher chance to contact the compartments as compared to orange ones.

# IV. ENZYME CONFINEMENT UNDER RIGID COMPARTMENTS WITH IRREGULAR SHAPES BASED ON CRYSTAL DEFECTS.

4.1. Classic co-crystallization to immobilize enzymes.

Co-crystallization of enzyme with certain metal ions and ligands can form enzyme@MOF biocomposites. 100-104 The involved enzymes often serve as the crystallization nuclei which can speed up the rate of co-crystal formation. The resultant "confinement" surrounding an enzyme is often in the shape of enzyme outline (like a scaffold on the surface of a building), and thus, considered as irregular confinement. The "scaffolds" are also rigid, which helps protecting/stabilizing the entrapped enzyme. While most published works were focused on the functionalities of the entrapped enzymes, there was a lack of structural and dynamic information of the enzymes, in particular, the area(s) of enzymes being exposed above co-crystals and the backbone dynamics (conformational equilibrium) upon immobilization in MOFs. This information is important for understanding how an enzyme recognizes and contacts substrates in the solvent or within MOF scaffolds. 105-110 The challenge is, again, probing enzyme structural and dynamic information under the interference of the MOF scaffolds (metal ions and ligands) using most protein-probing experimental techniques. We found that SDSL-EPR can overcome this barrier and offer residue-level information on enzyme backbone dynamics, and demonstrated this concept on our model enzyme, T4L, upon co-crystallization with Zn<sup>2+</sup> and imidazolate (T4L@ZIF-8 biocomposites).<sup>50</sup> In particular, we labeled multiple surface residues of T4L as in previous sections and co-crystallized each mutant with Zn<sup>2+</sup> and imidazolate. We found that each labeled surface site of T4L showed both a mobile and immobile spectral components, with the relative population varied drastically among different labeled sites (Figure 10A). We rationalized the presence of the mobile component as the labeled site being partially exposed above the ZIF-8 scaffold, indicating that a portion of the enzyme can be buried under the ZIF-8 scaffold surface while the rest of the enzyme can be exposed above it. This was also proved by the fact that large substrates (micrometer scale bacterial cell walls), which can never be able to diffuse into the ZIF-8 pores (0.6-0.7 nm),

can be degraded by the entrapped enzyme.<sup>50</sup> Upon spectral simulation, we were able to quantify the differences in the chance of exposing different T4L regions, based on which a few favored enzyme exposed sites above the MOF scaffold surface were proposed (Figure 10B). The partial exposure was also confirmed by urea perturbation, wherein the denaturant urea was only able to unfold protein portions above the MOF crystal surface (but not enzymes buried inside). The excellent consistency between the relative population of the mobile component from the simulation of the T4L@ZIF-8 and that of the mobile component from the urea disturbed T4L@ZIF-8 proved our speculation of the partial exposure of enzymes upon co-crystallization in MOFs.<sup>50</sup>

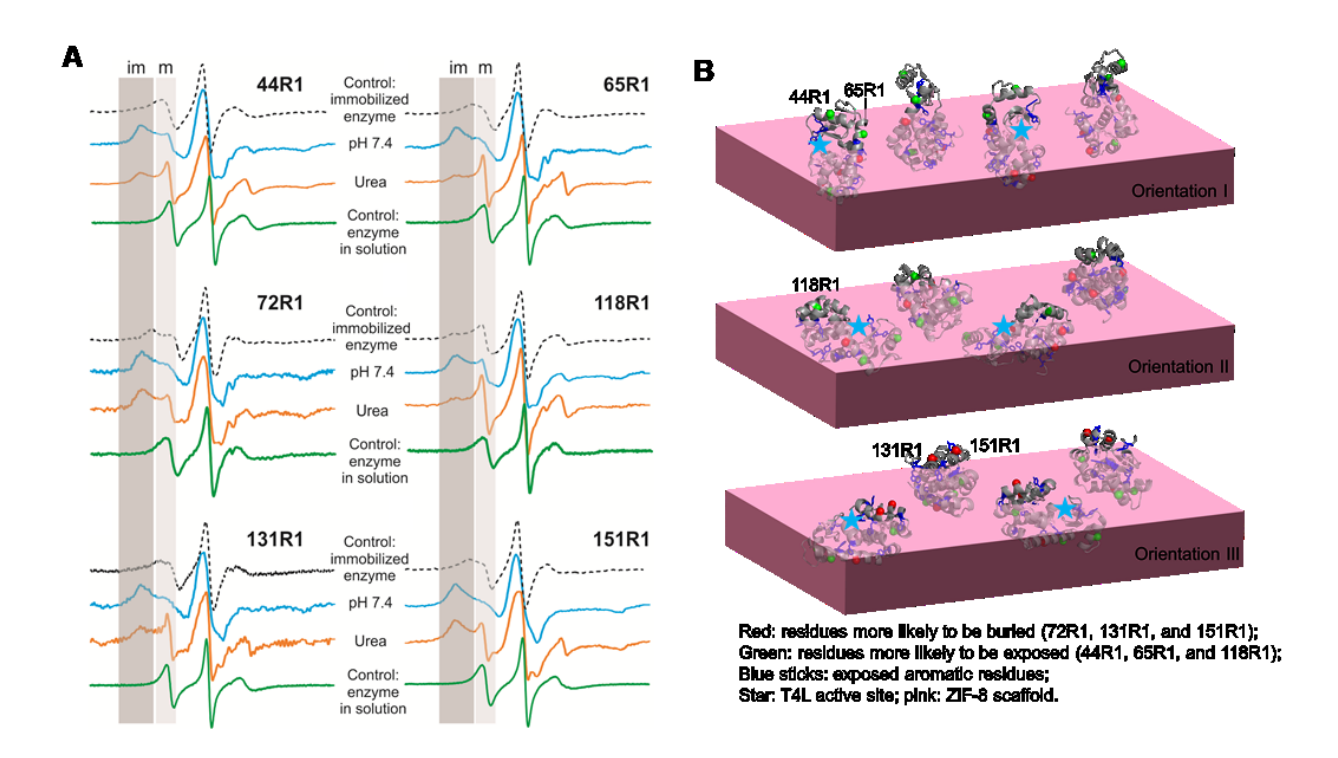


**Figure 10.** (A) CW EPR spectra of six surface sites spin labeled with an R1 sidechain at room temperature in varied conditions (dotted=immobilized enzyme; cyan=pH 7.4; orange=upon treatment with urea; green=free enzyme in solution). The field scan range is 3300 G to 3400 G.

(B) Three proposed exposed areas of the studied enzyme on the surface of ZIF-8. Reprinted

# (adapted) with permission from J. Am. Chem. Soc. 140, 16032 (2018). Copyright 2018 American Chemical Society.

A similar strategy was applied to 14 more combinations of metal ions and ligands, such as Ca-BDC, Ca-BPDC, Ca-NH<sub>2</sub>-BPDC, Ca-DDVA, and the combination of five ions ( $Zn^{2+}$ ,  $Cu^{2+}$ ,  $Ni^{2+}$ ,  $AI^{3+}$ , and  $Zr^{4+}$ ) with BDC/BPDC, wherein DDVA is a ligand extracted from natural product lignin while BDC and BPDC represent 1,4-benzendicarboxylic acid and biphenyl-4,4 - dicarboxylic acid, respectively.<sup>36, 38</sup> In the former four Ca-MOFs, we have published the proposed exposure regions of T4L on these MOFs. Interestingly, even for the enzymes buried under the MOF crystals, we found differences in backbone dynamics so that more freedom was found in Ca-NH<sub>2</sub>-BPDC as compared to that in Ca-BPDC, as indicated by the enhanced backbone dynamics (rate) of the immobile components in the former MOF (Figure 11).<sup>38</sup> Quantitative measurement of T4L catalytic efficiency in solution and upon immobilization resulted in different  $K_m$  and  $V_{max}$  parameters (Table 2 adapted from reference).<sup>38</sup> Depending on Ca-MOF selection, the catalytic efficiency of the confined enzyme is reduced from 77.8 % (Ca-NH<sub>2</sub>-BPDC) to 36.7 % (Ca-BPDC) as compared to the positive control (free enzyme).

**Table 2.** The kinetic parameters of cell wall degradation catalyzed by T4L and T4L confined in MOFs.

	$V_{max}$ (µmol/min)	$K_m(\mu M)$
T4L (control)	173.7 +/- 16.8	0.36 +/- 0.10
T4L@Ca-BDC	72.8 +/- 2.68	0.087 +/- 0.016
T4L@Ca-BPDC	63.8 +/- 3.8	0.130 +/- 0.036
T4L@Ca-NH <sub>2</sub> -BPDC	135.2 +/- 2.8	0.171 +/- 0.013

We also found a rough correlation between crystallinity and the rate of the motions of the mobile and immobile components in a series of MOFs formed by 4 ions and BDC/BPDC (8 MOFs total; manuscript under review). These works further confirmed the power of SDSL-EPR in probing the area(s) of enzymes being exposed above co-crystals and the backbone dynamics upon immobilization in MOFs. The information is important for guiding the rational design of new MOFs to co-crystallize/confine enzymes. It is worth noting that most of our co-crystallization reactions were carried out in water phase, which minimizes the damage to the target enzyme and removes the limitation on enzyme size and complexity (so that multiple enzyme clusters can be co-immobilized together).

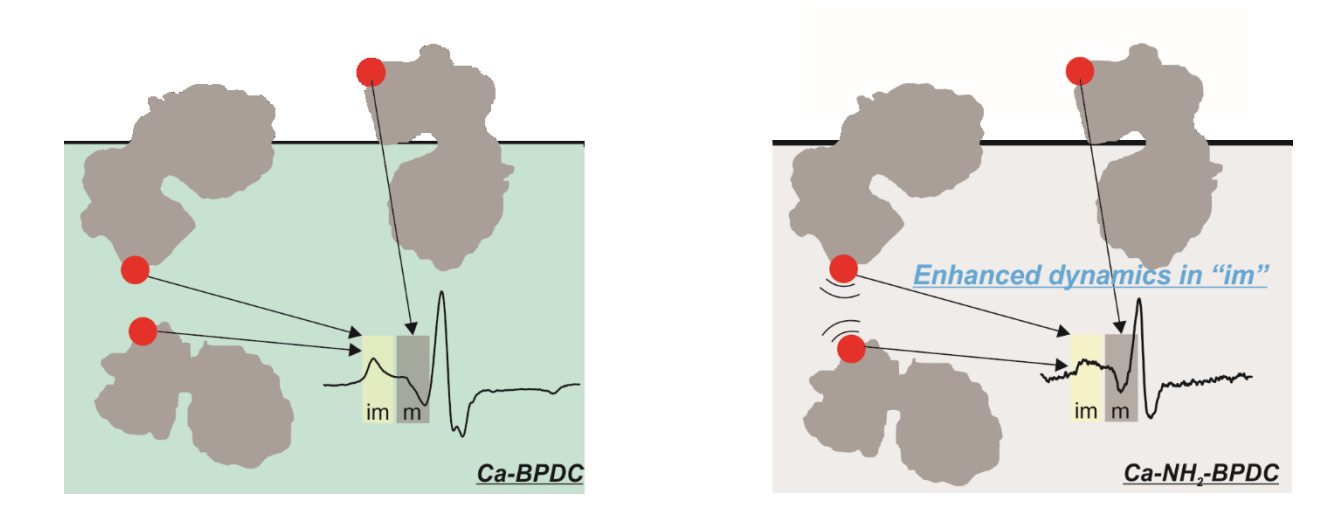


Figure 11. Difference in the immobile component of the CW EPR spectra for T4L in Ca-BPDC and Ca-NH<sub>2</sub>-BPDC at room temperature can be detected and quantified to report the dynamics of the entrapped enzyme sidechain in different MOF crystal scaffolds. The field scan range is 3300 G to 3400 G for both spectra. Reprinted (adapted) with permission from Chem Catal. 1, 207 (2021). Copyright 2021 Elsevier.

### 4.2. Advanced co-crystallization platforms to provide advanced functionalities.

We have also developed experimental strategies to endorse more functions to the enzyme co-crystallized with MOFs and probed the enzyme contact with MOF and exposure. For example, we found that enzymes and metal ions/ligands can be co-crystallized on the surface of carbon nanotubes (CNTs), which offers enhanced chance to expose enzyme regions likely due to the occupancy of the MOFs space by CNTs (so that less enzymes can occupy the interior space of the MOFs).<sup>47</sup> Interestingly, the resultant enzyme@MOF/CNTs composites are stable under acidic pHs, which is opposite to the general properties of ZIF-8 which are not stable under acidic pHs. <sup>47</sup> Also, graphene oxides (GOs) can serve as the seed to co-crystallize enzymes and MOFs. 45 We have also attempted to endorse magnetic properties to enzyme@MOFs composites to enhance the separation efficiency after biocatalytic reactions, although probing the exposure information by EPR is challenging due to the presence of the magnetic nanoparticles which severely interfere with EPR signal detection. 44 We have also proved the effectiveness of co-immobilizing multiple enzymes on the same MOF to promote the biocatalytic efficiency.<sup>42</sup> In particular, the time to degrade a model cereal substrate (essentially a food sample) using three digestive enzymes, α-amylase, amyloglucosidase, and protease, sequentially following the classic procedure in food industry was ~155 min, while co-immobilizing multiple enzymes on the same MOF reduced the degradation time to ~50 min.42 The catalytic time was reduced by a factor of ~3! Studies on the exposure/contact and dynamics of the immobilized enzymes in these multi-enzyme@MOF composites are underway.

A unique case study was to immobilize a protease on MOFs via co-crystallization, which minimized the self-degradation of protease during a function/mechanism study. Proteases hydrolyze peptide bonds at specific residues/sequences and thus, are essential for cellular functions. However, it is challenging to study the interactions between protease and

substrates using most experimental approaches. In a recent work, we labeled a protein substrate via SDSL and used time-resolved, 2D CW EPR to monitor the lineshape changes over time upon contact with trypsin, a model serine protease (Figure 12A).<sup>52</sup> The advantage of EPR is that the presence of trypsin and broken pieces of the substrate did not affect the CW EPR signal. The further the proteolytic reaction proceeded, the smaller the labeled protein segment, and the sharper the linewidth (Figure 12B). By spectral simulation, we were able to determine the changes in the populations of the broken substrate pieces over time, which can suggest the possible preference of the cleavage site on the model substrate (Figure 12C). We noted that the EPR results cannot be confirmed by mass spectrometry (MS), which is a typical technique to study proteolytic reactions, because the reaction cannot be conveniently quenched to obtain time-resolved MS data.<sup>52</sup> Thus, we immobilized trypsin on a MOF, Ca-BPDC, so that the products can be separated from the insoluble, trypsin@Ca-BPDC composites and subjected to EPR and MS study (Figures 12D and 12E). Remarkably, MS and EPR resulted in amazingly consistent findings on the preference of cleavage site and cleavage kinetics.<sup>52</sup>

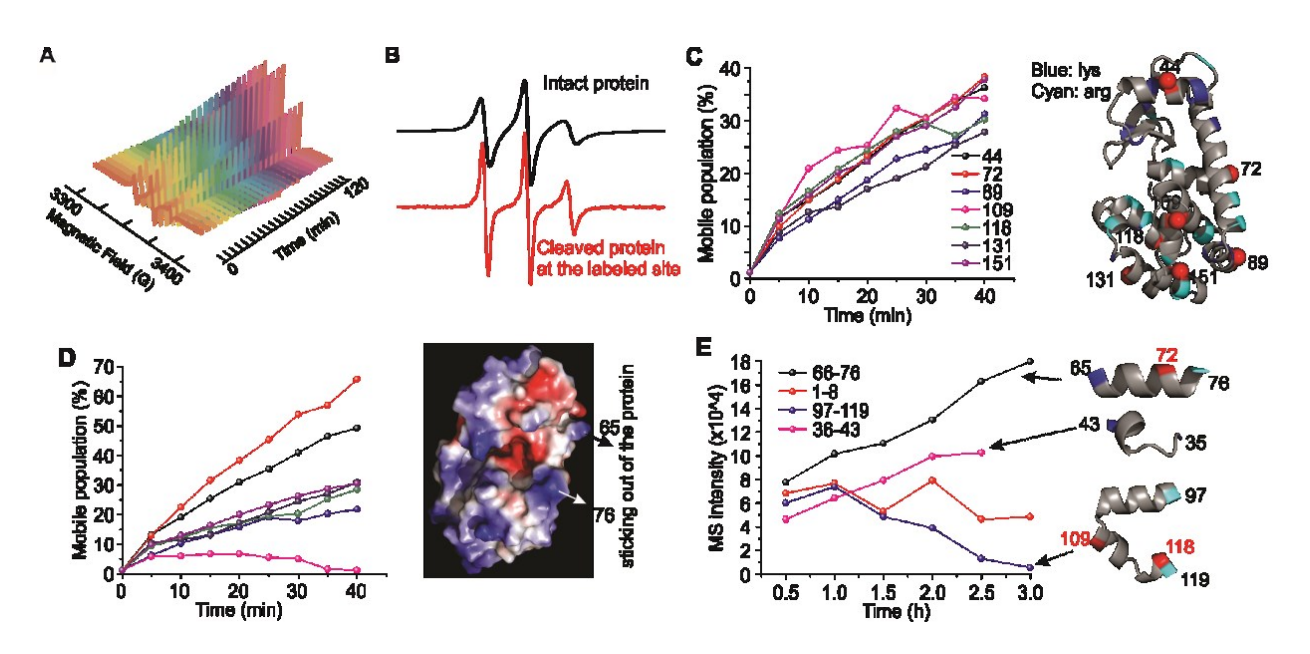


Figure 12. (A) Typical time-resolved EPR data to probe the degradation of a spin labeled protein substrate, T4L, by trypsin in HEPES buffer at room temperature. (B) Spectral difference between intact and cleaved T4L by free trypsin in HEPES buffer at room temperature. The field scan range is 3300 G to 3400 G. (C) Near zero selectivity of free trypsin against a protein substrate T4L in HEPES buffer due to the similar increase rate in the population of broken pieces; cleavage sites of trypsin are shown on the right. (D) Certain T4L sites such as 72 and 44 were degraded faster than others due to their exposed cleavage sites (right) with trypsin@Ca-BPDC.

(E) MS data supported the cleaved pieces indicated by EPR (right).

# V. POLYPEPTIDE CONFINEMENT UNDER FLEXIBLE, DYNAMIC CONFINEMENT BASED ON POLYMERIC MATERIALS.

### 5.1. Polypeptides as probes to sense polymeric micelle interior environments.

Polymeric micelles find wide applications as molecular delivery vehicles and platforms to mimic the crowded/confined cellular environment, yet there is a lack of effort on probing the interior environment of micelles and the entrapped molecular cargos. 116-119 Knowing the interior of a micelle, in particular the polarity and crowding extent inside of micelles which can likely affect cargo's location, aggregation state, and possibly structure if the cargo is a (bio)macromolecule, is important for not only predicting the performance of the molecular cargos but also guiding the rational design of novel micelles to better mimic the cellular environment. Probing the interior of a micelle, however, is a challenging task, due to the interference of the polymeric molecules and their dynamic interactions (when forming a micelle). We have utilized spin labeled polymers and CW EPR to probe the interface of the hydrophilic shell and hydrophobic core of a series of polymeric micelles formed by diblock polymers (Polyethylene glycol-

Polycaprolactone, or, PEG-PCL) with different core sizes.<sup>51</sup> We found that the spin label attached at the interface between the PEG and PCL segments showed two components (Figure 13A), likely due to the fact that the spin labels in these labeled molecules can partially point to the hydrophilic shell and partially be trapped in the hydrophobic core, which resulted in a relatively mobile motion and highly restricted motion, respectively. The percentage of the labels in restricted motion is dependent on the length of PCL, so that the longer the PCL segment, the more restriction to the motion (28+/-3, 33+/-5, and 31+/-3 % of the immobile components for PCL segment with 2000, 9000, and 11000 molecular weight, respectively). We also probed the disassembly of the micelle by a typical organic solvent, tetrahydrofuran (THF), so that the more THF was present, the less restriction of the motion of the label (Figure 13B). This work was a demonstration of the sensitivity of EPR on micelle dynamics and interior environment.<sup>51</sup>

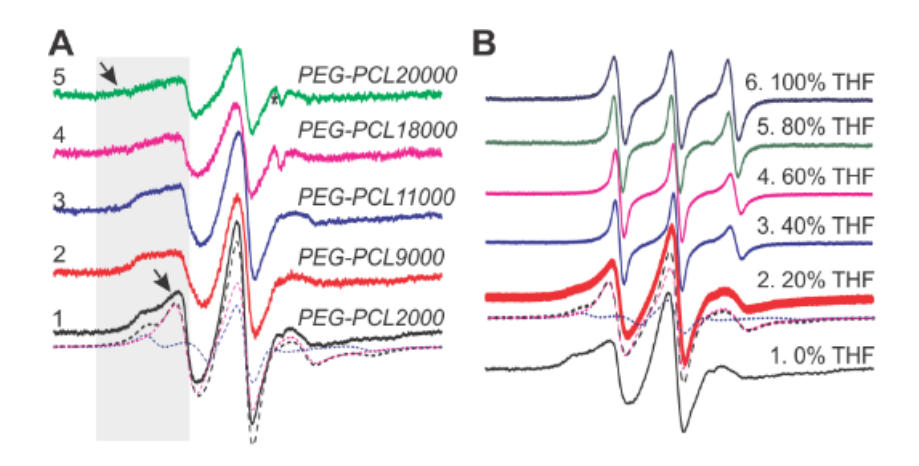


**Figure 13.** (A) CW EPR spectra of PEG-PCL spin labeled at the connection between the two blocks at room temperature. (B) THF disassembles the PEG-PCL micelles as probed and reported by the narrowing CW EPR spectra at room temperature. The field scan range is 3300 G to 3400 G in all spectra.

We also non-selectively spin labeled an antigenic glycoprotein hemagglutinin (HA) polypeptide (Figure 14A), and utilized EPR to probe the motion of the HA peptide, which was believed to be dependent on the local environment of the interior of the micelle. We chose two micelles, a regular micelle (S10) formed by a classic diblock polymer and an invertible micelle assembly (IMA) based on repeating units of PEG-PTHF (Figure 14B). We found that the two micelles displayed different "tightness" upon disturbance by acetone so that the mobile component in the IMAs was lower than that in S10 under the same acetone concentration, suggesting that IMAs have a higher packing stability against external disturbance (Figure 14 C&D). This work also proved the power of EPR on probing the interior of micelles.

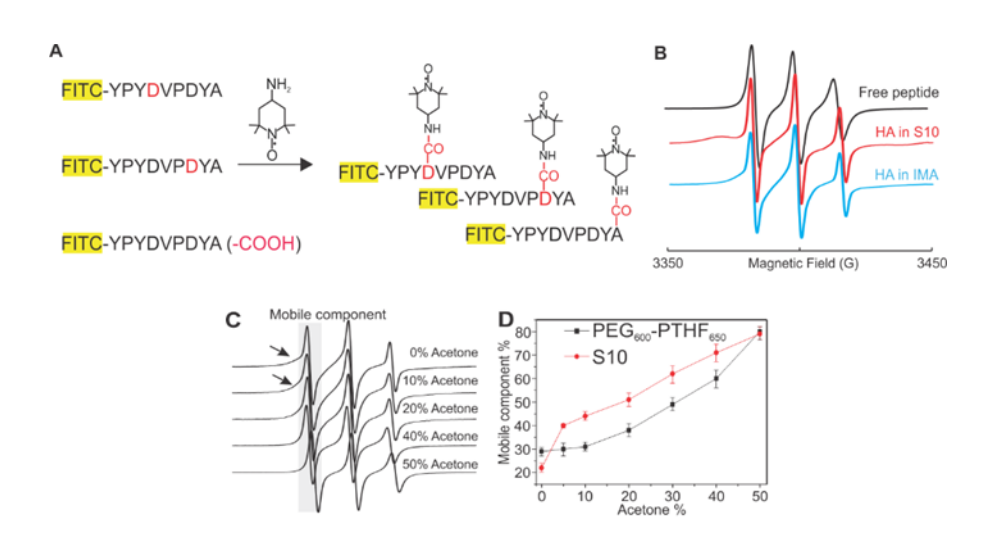


Figure 14. (A) Non-selective HA peptide labeling results in a random labeling position. (B) EPR spectra of the randomly labeled peptide in solvent, S10, and another IMA(PEG<sub>600</sub>-PTHF<sub>650</sub>) at room temperature. (C) CW EPR spectra of non-selectively spin labeled HA peptide upon disassembly by acetone. (D) The percentage of the mobile component, which indicates the extent of disassembly, as a function of acetone percentage. Reprinted (adapted) with permission from J. Phys. Chem. C 122, 25692 (2018). Copyright 2018 American Chemical Society.

# 5.2. Polypeptide dynamics and aggregation upon confinement in advanced micellar materials.

We also selectively labeled the same HA peptide at the head, middle, and tail/end positions (Figure 15A) and monitored the relative local polarity and crowding changes for the same model IMA, PEG-PTHF, upon addition of acetone and inversion caused by toluene. 43 In water, we observed the expected line broadening as the labeled site was moved to the more crowded interior of the IMA, due to the enhanced restriction in motion at the labeled region of the peptide (Figure 15B). Then, we inverted the polarity of the solvent by dialyzing against toluene and observed the opposite location of the labeled regions of the HA peptide (so that the hydrophobic head was located at the shell while the more hydrophilic tail was buried inside of the core). We also observed peptide aggregation inside of the inverted IMA so that CW EPR was utilized to determine the distances among three labeled HA peptide residues, one at a time. We then established the average distances among the aggregated peptides at each labeled position and found that the "head" of the peptide tends to aggregate closer to each other as compared to the "tail" of the peptide in toluene, based on which an aggregation state model was proposed for the HA peptide in IMA (Figure 15 C&D).<sup>43</sup> This work is important for understanding the behavior of large biomolecular cargos in micelles, shedding light on the rational design of advanced micelles for optimal drug delivery performance and mimicking the cellular organelles using the crowded, soft confinement offered by polymeric materials. For example, based on cargo location, aggregation states, and movement upon solvent polarity change determined by EPR, one could assess if a cargo molecule is placed at the desired location (core or shell of the micelle) and predict the movement and release of the cargo from the micelle. If the cargo location is not ideal in the micelle and/or the cargo cannot be released from the micelle, then, fine-tuning of the lengths and hydrophobicity of the micelle'

hydrophobic and hydrophilic segments can be carried out to adjust cargo location and release, which will be assessed through another round of EPR measurement.

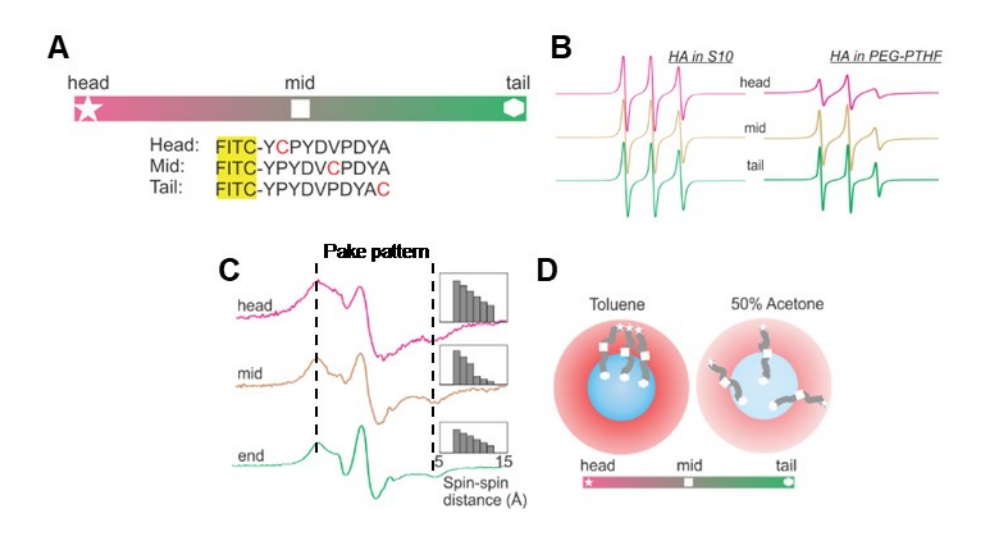


Figure 15. (A) Cysteine insertion to control the labeling position in HA. (B) EPR spectra of the HA peptide labeled at different positions in S10 and PEG<sub>600</sub>-PTHF<sub>650</sub> at room temperature. Scan range is 3300 to 3400 G. (C) Experimental room temperature CW EPR data (scan range 150 G centered at ~3400 G) show different lineshapes which are composed of the regular three-line splitting of nitroxides as well as the Pake pattern (as guided by the dotted lines) due to the spin-spin magnetic dipolar interactions under close spin proximity caused by aggregation. The estimated distance distribution among spin labels at the head, mid, and end/tail positions of the peptide are shown in the inset of each. (D) Schematic illustration of the proposed aggregation states of the labeled HA peptide in IMAs in toluene and 50 % acetone. Reprinted (adapted) with permission from ACS Appl. Mater. Interfaces 12, 12075 (2020). Copyright 2020 American Chemical Society.

## 5.3. Polymer shells conjugated to enzyme surfaces.

The original motivation of conjugating soluble polymers to enzyme surfaces was to create permeant confinement (as compared to loading polypeptides into micelles and the potential leaching) and thus, long-lasting protection to the target enzymes and endorsing polymeric functions/properties to the host protein, with the ultimate applications in enzyme stabilization and delivery. 124-128 We chose the biocompatible polymer PEG with different lengths and reacted these PEGs with protein lysines (amines) under different feeding ratio (PEG-to-protein ratio).<sup>49</sup> The resultant conjugate complexes were believed to be highly heterogeneous in molecular weight and conjugation sites, making it challenging to probe the molecular level enzyme structure and dynamics information. We utilized EPR and SDSL to probe these details. First, we found that the size and abundance (determined by feeding ratio) affect the catalytic efficiency of the modified T4L by influencing the accessibility of the substrate to the enzyme active site (Figure 16 A&B). In particular, the catalytic efficiency was assessed by a classic lysozyme activity assay, wherein the degradation of bacterial cell walls resulted in a decrease in the optical density at 450 nm (OD450). The relative slope of OD450 drop over time was quantified as an assessment to enzyme activity. For PEG with a 5k molecular weight, the slope of OD450 drop is ~50 % of the wildtype protein at low feeding ratios (100-150:1). At higher feeding ratios (250-500:1), there is almost no activity observed. Similar trends hold for PEG with a 20k molecular weight, wherein hybrids prepared with a 25:1 and a 100:1 ratio showed ~45 % and 25 % of the catalytic efficiency of the wildtype enzyme. Comparing PEG with a 5k and 20k at the same feeding ratio suggested that the longer the PEG chain, the lower the catalytic efficiency (~45 % vs ~50 % of the wildtype activity). At 500:1, PEG with a molecular weight of 1.9k showed almost no activity, indicating the more the protein amines occupied, the less the activity, even if the polymer chain is relatively short. To understand this, we probed the structural basis of the resultant conjugates. We found that an

increase in linewidth as the feeding ratio and/or size of PEG was increased for most labeled sites, which is consistent with the enhanced linewidth due to the enhanced molecular weight upon increasing the amount of PEG conjugated to the protein (Figure 16 C&D green vs black curves). Because the lineshape is dependent on the rotational correlation time of the whole protein-polymer conjugate, which further depends on the overall molecular weight, we utilized spectral simulation to extract the rotational correlation time and computed the average molecular weight of each conjugate. We found a rough correlation between the calculated molecular weight and the molecular weight distribution by electrophoresis as detailed in our work. The exceptions are two sites, 44 and 131, which did not show the expected linewidth increase even under the highest feeding ratio with the longest PEG (Figure 16 C&D orange). We rationalized this finding to the local disruption to the target enzyme, T4L, due to the conjugation of PEGs near these sites. Given the high abundance of lysines near these two sites, this rationalization is reasonable. This work is a clear demonstration of the use of SDSL-EPR in probing enzyme performance inside of a soft but stable polymer shell.

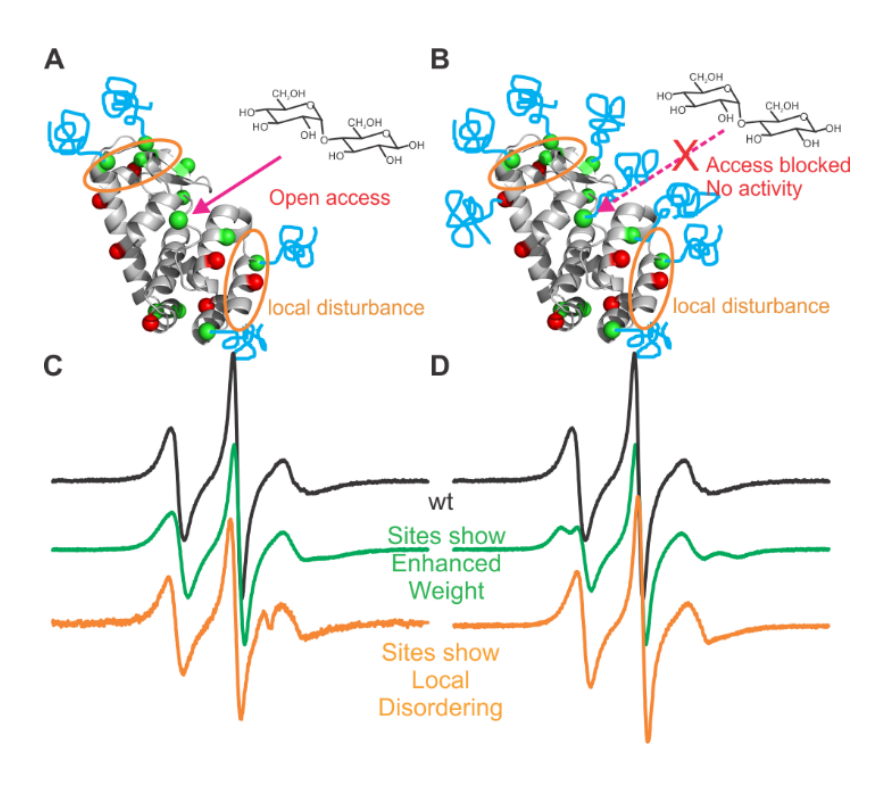


Figure 16. Illustrations of low (A) and high (B) polymer abundance in a conjugate and their influence on local dynamics determined by EPR at room temperature (C,D). In (A) and (B), the red spheres represent the α-carbon of the labelled residues for the dynamics studies while the green spheres indicate the distribution of lysine which can react with the polymer. The extent of EPR spectral broadening is correlated with polymer abundance (green curves of C and D are data from residues 65R1 and 72R1) while local disordering narrows the linewidth on certain sites (orange curves of C and D are data from residues 44R1 and 131R1). The field scan range is 3300 G to 3400 G.

## VI. CONCLUDING REMARKS AND OUTLOOK

Aiming at promoting biocatalyst design and fundamental protein biophysics under spatial confinement, we have developed various confinement conditions which an enzyme could encounter naturally or artificially and examined enzyme performance using SDSL in combination

with EPR spectroscopy. We found that by diffusion, enzyme can be immobilized in pre-formed compartment materials with rigid, regular shapes. The performance of the T4L enzyme, which can be quantified by various parameters (such as enzymatic kinetics parameters, absorption decrease at a certain wavelength, or time to degrade the same model substrate) and relies on the interplay of the structure, dynamics, and function, depends on the restriction to the conformational degree of freedom upon confinement. CW EPR offers a powerful way to determine the strength of the contact between a protein residue and the compartment surface as well as the relative protein contact regions with respect to the confinement surface. The substrates have to be limited to those smaller than the pore size of the compartment materials. In addition, by co-crystallization, enzyme can be implanted on the surface of MOF crystals so that certain regions of the enzyme can be exposed above the crystal surface, which promotes the biocatalysis involving substrates larger than MOF pores. The exposed regions can also be determined by CW EPR. Enzymes partially exposed above the MOF crystal surface obviously display enhanced backbone dynamics as compared to those completely immobilized in the pre-formed MOFs/COFs. Enzymes buried inside of the cocrystals could also have different backbone motions depending on the MOF scaffolds. Lastly, under "soft" confinement environment, spin labeled polypeptides can report the interior (local) environment of the polymeric micelles upon EPR measurement, a unique advantage to probe the interiors of self-assemblies, while polymers conjugated to enzymes affect the molecular weight and the local ordering, which can also be detected by EPR. These findings can serve as the guidance of the selection of enzyme confinement platforms for various applications and generate excitement in the community of protein biophysics, biocatalysis, and biochemistry on combining cutting-edge materials and experimental technologies to better understand enzyme performance in biophysics, biocatalysis, and biomedical applications.

In the future, intra-distance measurements in the entrapped enzymes using advanced, pulsed EPR techniques such as double electron-electron resonance (DEER) and double quantum coherence (DQC) should be carried out to provide more thorough pictures of the global structural changes of the entrapped enzyme in the absence and presence of substrates under varied confinement environment. Also, more enzymes need to be studied via SDSL-EPR upon confinement under varied compartment materials depending on the application. The structure-based enzyme immobilization/confinement design will likely promote the rational design of enzyme confinement platforms.

#### **ACKNOWLEDGEMETNS**

The authors gratefully acknowledge funding support from the National Science Foundation, Grant No. MCB 1942596, CBET 2217474, and DMR 2306137.

## **DATA AVAILABILITY**

Data sharing is not applicable to this article as no new data were created or analyzed.

#### **REFERENCES**

- 1. S. J. Benkovic and S. Hammes-Schiffer, Science **301** (5637), 1196-1202 (2003).
- 2. U. Hanefeld, L. Gardossi and E. Magner, Chem. Soc. Rev. 38 (2), 453-468 (2009).
- 3. O. Kirk, T. V. Borchert and C. C. Fuglsang, Curr. Opin. Biotechnol. **13** (4), 345-351 (2002).
- 4. X. Wang, P. C. Lan and S. Ma, ACS Centr. Sci. 6, 1497-1506 (2020).
- 5. J. Mehta, N. Bhardwaj, S. K. Bhardwaj, K. H. Kim and A. Deep, Coord. Chem. Rev. **322**, 30-40 (2016).
- 6. M. Hartmann and X. Kostrov, Chem. Soc. Rev. **42** (15), 6277-6289 (2013).
- 7. N. R. Mohamad, N. H. C. Marzuki, N. A. Buang, F. Huyop and R. A. Wahab, Biotechnol. Biotechnol. Equip. **29** (2), 205-220 (2014).
- 8. J. M. Bolivar, I. Eisl and B. Nidetzky, Catal. Today **259**, 66-80 (2016).
- 9. C. Garcia-Galan, Á. Berenguer-Murcia, R. Fernandez-Lafuente and R. C. Rodrigues, Adv. Syn. Catal. **353** (16), 2885-2904 (2011).
- 10. T. Jesionowski, J. Zdarta and B. Krajewska, Adsorption **20** (5), 801-821 (2014).
- 11. E. R. Georgieva, *Molecules* **25**, 5393. doi: 10.3390/molecules25225393 (2020),
- 12. D. Otzen, Biochim. Biophys. Acta BBA Proteins Proteom. **1814** (5), 562-591 (2011).
- 13. A. M. Seddon, P. Curnow and P. J. Booth, Biochim. Biophys. Acta BBA Biomembr. **1666** (1), 105-117 (2004).
- 14. F. Cymer, G. von Heijne and S. H. White, J. Mol. Biol. **427** (5), 999-1022 (2015).
- 15. M. Stefani, *Inter. J. Mol. Sci.* **9**, 2515-2542. (2008).
- 16. R. A. Hartvig, M. van de Weert, J. Østergaard, L. Jorgensen and H. Jensen, Langmuir 27 (6), 2634-2643 (2011).

- 17. J. J. Gray, Curr. Opin. Struct. Biol. 14 (1), 110-115 (2004).
- 18. K. Nakanishi, T. Sakiyama and K. Imamura, J. Biosci. Bioengineer. **91** (3), 233-244 (2001).
- 19. Y. Pan, S. Neupane, J. Farmakes, M. Bridges, J. Froberg, J. Rao, S. Y. Qian, G. Liu, Y. Choi and Z. Yang, Nanoscale 9, 3512-3523 (2017).
- 20. R. J. Drout, L. Robison and O. K. Farha, Coord. Chem. Rev. **381**, 151-160 (2019).
- 21. P. Li, Q. Chen, T. C. Wang, N. A. Vermeulen, B. L. Mehdi, A. Dohnalkova, N. D. Browning, D. Shen, R. Anderson, D. A. Gómez-Gualdrón, F. M. Cetin, J. Jagiello, A. M. Asiri, J. F. Stoddart and O. K. Farha, Chem 4 (5), 1022-1034 (2018).
- 22. M. B. Majewski, A. J. Howarth, P. Li, M. R. Wasielewski, J. T. Hupp and O. K. Farha, CrystEngComm **19** (29), 4082-4091 (2017).
- 23. E. Gkaniatsou, C. m. Sicard, R. m. Ricoux, J.-P. Mahy, N. Steunou and C. Serre, Mater. Horiz. 4 (1), 55-63 (2017).
- 24. X. Lian, Y. Fang, E. Joseph, Q. Wang, J. Li, S. Banerjee, C. Lollar, X. Wang and H.-C. Zhou, Chem. Soc. Rev. **46** (11), 3386-3401 (2017).
- 25. E. J. Sorin and V. S. Pande, J. Am. Chem. Soc. **128** (19), 6316-6317 (2006).
- 26. C.-H. Lee, T.-S. Lin and C.-Y. Mou, Nano Today 4 (2), 165-179 (2009).
- W. Wang, W.-X. Xu, Y. Levy, E. Trizac and P. G. Wolynes, Proc. Natl. Acad. Sci. 106
   (14), 5517 (2009).
- 28. M. L. Ross, J. Kunkel, S. Long and P. Asuri, Int. J. Mol. Sci. **21** (22) (2020).
- 29. S. Datta, L. R. Christena and Y. R. S. Rajaram, 3 Biotech **3** (1), 1-9 (2013).
- 30. R. C. Rodrigues, C. Ortiz, Á. Berenguer-Murcia, R. Torres and R. Fernández-Lafuente, Chem. Soc. Rev. **42** (15), 6290-6307 (2013).

- 31. Z. Zhou and M. Hartmann, Chem. Soc. Rev. **42** (9), 3894-3912 (2013).
- 32. N. Carlsson, H. Gustafsson, C. Thörn, L. Olsson, K. Holmberg and B. Åkerman, Adv. Colloid Interface Sci. **205**, 339-360 (2014).
- 33. P. Li, J. A. Modica, A. J. Howarth, E. Vargas L, P. Z. Moghadam, R. Q. Snurr, M. Mrksich, J. T. Hupp and O. K. Farha, Chem **1** (1), 154-169 (2016).
- 34. Y. Pan, Q. Li, W. Liu, Z. Armstrong, A. MacRae, L. Feng, C. McNeff, P. Zhao, H. Li and Z. Yang, Nanoscale **15** (6), 2573-2577 (2023).
- Y. Pan, Q. Li, H. Li, M. Lenertz, D. Jordahl, Z. Armstrong, B. Chen and Z. Yang, J.
   Magn. Reson. Open 10-11, 100060 (2022).
- D. Jordahl, Z. Armstrong, Q. Li, R. Gao, W. Liu, K. Johnson, W. Brown, A. Scheiwiller,
   L. Feng, A. Ugrinov, H. Mao, B. Chen, M. Quadir, Y. Pan, H. Li and Z. Yang, ACS Appl.
   Mater. Interfaces 14 (46), 51619-51629 (2022).
- 37. Y. Pan, X. Wang, H. Li, J. Farmakes, I. Schuster, D. Jordahl, H. Hong, Z. Yang and S. Ma, Cell Rep. Phys. Sci. 2, 100576 (2021).
- 38. Y. Pan, Q. Li, H. Li, J. Farmakes, A. Ugrinov, X. Zhu, Z. Lai, B. Chen and Z. Yang, Chem Catal. 1, 146-161 (2021).
- 39. Y. Pan, H. Li, Q. Li, M. Lenertz, X. Zhu, B. Chen and Z. Yang, Chem Catal. 1, 207-231 (2021).
- 40. Y. Pan, H. Li, Q. Li, M. Lenertz, I. Schuster, D. Jordahl, X. Zhu, B. Chen and Z. Yang, STAR Protoc. **2** (3), 100676 (2021).
- 41. Y. Pan, H. Li, M. Lenertz, Y. Han, A. Ugrinov, D. Kilin, B. Chen and Z. Yang, Green Chem. **33**, 4466-4476 (2021).

- 42. Q. Li, Y. Pan, H. Li, M. Lenertz, K. Reed, D. Jordahl, T. Bjerke, A. Ugrinov, B. Chen and Z. Yang, ACS Appl. Mater. Interfaces 13, 43085–43093 (2021).
- 43. Y. Pan, O. Zholobko, H. Li, J. Jin, J. Hu, B. Chen, A. Voronov and Z. Yang, ACS Appl. Mater. Interfaces 12, 12075-12082 (2020).
- 44. Q. Li, Y. Pan, H. Li, L. Alhalhooly, Y. Li, B. Chen, Y. Choi and Z. Yang, ACS Appl. Mater. Interfaces 12, 41794-41801 (2020).
- 45. J. Farmakes, I. Schuster, A. Overby, L. Alhalhooly, M. Lenertz, Q. Li, A. Ugrinov, Y. Choi, Y. Pan and Z. Yang, ACS Appl. Mater. Interfaces **12** (20), 23119-23126. (2020).
- 46. Q. Sun, Y. Pan, X. Wang, H. Li, J. Farmakes, B. Aguila, Z. Yang and S. Ma, Chem 5 (12), 3184-3195 (2019).
- 47. S. Neupane, K. Patnode, H. Li, K. Baryeh, G. Liu, J. Hu, B. Chen, Y. Pan and Z. Yang, ACS Appl. Mater. Interfaces **11** (12), 12133-12141 (2019).
- 48. Y. Pan, O. Zholobko, A. Voronov and Z. Yang, J. Phys. Chem. C **122**, 25692-25699 (2018).
- 49. Y. Pan, S. Neupane, J. Farmakes, M. Oh, K. Bentz, Y. Choi and Z. Yang, ChemPhysChem **19** (5), 651-658 (2018).
- Y. Pan, H. Li, J. Farmakes, F. Xiao, B. Chen, S. Ma and Z. Yang, J. Am. Chem. Soc.
   140, 16032-16036 (2018).
- 51. Y. Pan, S. Neupane, J. Farmakes, B. Liu, W. Sun and Z. Yang, J. Polym. Sci. B Polym. Phys. 55, 1770-1782 (2017).
- 52. Q. Li, Z. Armstrong, A. Ugrinov, B. Chen, B. Liu, H. Li, Y. Pan and Z. Yang, ACS Appl. Mater. Interfaces 15 (7), 8927-8936 (2022).

- 53. H. Li, Y. Pan, J. Farmakes, F. Xiao, J. Hu, B. Chen, J. Rao and Z. Yang, J. Colloid Interface Sci. **556**, 292-300 (2019).
- O. Schiemann, C. A. Heubach, D. Abdullin, K. Ackermann, M. Azarkh, E. G.
   Bagryanskaya, M. Drescher, B. Endeward, J. H. Freed, L. Galazzo, D. Goldfarb, T. Hett, L.
   Esteban Hofer, L. Fábregas Ibáñez, E. J. Hustedt, S. Kucher, I. Kuprov, J. E. Lovett, A. Meyer,
   S. Ruthstein, S. Saxena, S. Stoll, C. R. Timmel, M. Di Valentin, H. S. McHaourab, T. F. Prisner,
   B. E. Bode, E. Bordignon, M. Bennati and G. Jeschke, J. Am. Chem. Soc. 143 (43), 17875-17890 (2021).
- 55. D. S. Cafiso, Acc. Chem. Res. 47 (10), 3102-3109 (2014).
- 56. T. Prisner, M. Rohrer and F. MacMillan, Ann. Rev. Phys. Chem. **52** (1), 279-313 (2001).
- 57. R. Davydov and B. M. Hoffman, Arch. Biochem. Biophys. **507** (1), 36-43 (2011).
- 58. G. Jeschke, Biochim. Biophys. Acta BBA Bioenerget. 1707 (1), 91-102 (2005).
- 59. W. L. Hubbell, C. J. López, C. Altenbach and Z. Yang, Curr. Opin. Struct. Biol. **23** (5), 725-733 (2013).
- 60. W. L. Hubbell, D. S. Cafiso and C. Altenbach, Nat. Struct. Biol. 7, 735 739 (2000).
- 61. W. L. Hubbell, A. Gross, R. Langen and M. A. Lietzow, Curr. Opin. Struct. Biol. **8** (5), 649-656 (1998).
- 62. G. E. Fanucci and D. S. Cafiso, Curr. Opin. Struct. Biol. 16 (5), 644-653 (2006).
- 63. M. R. Fleissner, E. M. Brustad, T. Kálai, C. Altenbach, D. Cascio, F. B. Peters, K. Hideg, S. Peuker, P. G. Schultz and W. L. Hubbell, Proc. Natl. Acad. Sci. **106** (51), 21637-21642 (2009).
- 64. A. P. Todd, J. Cong, F. Levinthal, C. Levinthal and W. L. Hubbell, Prot. Struct. Funct. Bioinform. 6 (3), 294-305 (1989).

- 65. I. D. Sahu and G. A. Lorigan, BioMed Res. Int. **2018**, Article ID 3248289 (2018).
- 66. H. Xiao and P. G. Schultz, Cold Spring Harb. Perspect. Biol. 8 (9) (2016).
- 67. C. Lopez, Doctor of Philosophy Thesis, https://escholarship.org/uc/item/5r00c82c University of California, Los Angeles, 2012.
- 68. D. E. Budil, S. Lee, S. Saxena and J. H. Freed, J. Magn. Reson. A **120** (2), 155-189 (1996).
- 69. S. Stoll and A. Schweiger, J. Magn. Reson. **178** (1), 42-55 (2006).
- 70. Z. Armstrong, A. MacRae, M. Lenertz, Q. Li, K. Johnson, A. Scheiwiller, P. Shen, L. Feng, M. Quadir and Z. Yang, ACS Appl. Mater. Interfaces **15** (31), 38124-38131 (2023).
- 71. L. Columbus and W. L. Hubbell, Biochemistry **43** (23), 7273-7287 (2004).
- C. J. López, M. R. Fleissner, Z. Guo, A. K. Kusnetzow and W. L. Hubbell, Prot. Sci. 18
   (8), 1637-1652 (2009).
- 73. K. Keller, I. Ritsch, H. Hintz, M. Hülsmann, M. Qi, F. D. Breitgoff, D. Klose, Y. Polyhach, M. Yulikov, A. Godt and G. Jeschke, Phys. Chem. Chem. Phys. **22** (38), 21707-21730 (2020).
- 74. B. E. Bode, J. Plackmeyer, M. Bolte, T. F. Prisner and O. Schiemann, J. Organometal. Chem. **694**, 1172-1179 (2009).
- 75. Y. N. Molin, K. M. Salikhov and K. I. Zamaraev, *Spin Exchange*. (Springer-Verlag, Berlin, 1980).
- 76. A. Weber, O. Schiemann, B. Bode and T. F. Prisner, J. Magn. Reson. **157** (2), 277-285 (2002).

- 77. K. Keller, I. Ritsch, H. Hintz, M. Hülsmann, M. Qi, F. D. Breitgoff, D. Klose, Y. Polybach, M. Yulikov, A. Godt and G. Jeschke, Phys. Chem. Chem. Phys. **Advance Article** (2020).
- 78. M. Margittai and R. Langen, Proc. Natl Acad. Sci. U. S. A. **101** (28), 10278-10283 (2004).
- 79. M. Chen, M. Margittai, J. Chen and R. Langen, J. Biol. Chem. **282** (34), 24970-24979 (2007).
- 80. T. Vöpel, C. S. Hengstenberg, T.-O. Peulen, Y. Ajaj, C. A. M. Seidel, C. Herrmann and J. P. Klare, Biochemistry **53** (28), 4590-4600 (2014).
- 81. O. Iyalomhe, D. Z. Herrick, D. S. Cafiso and P. C. Maloney, Biochemistry **53** (49), 7735-7744 (2014).
- 82. I. D. Sahu, A. F. Craig, M. M. Dunagum, R. M. McCarrick and G. A. Lorigan, J. Phys. Chem. B **121** (39), 9185-9195 (2017).
- 83. C. Abé, F. Dietrich, P. Gajula, M. Benz, K.-P. Vogel, M. van Gastel, S. Illenberger, Wolfgang H. Ziegler and H.-J. Steinhoff, Biophys. J. **101** (7), 1772-1780 (2011).
- 84. L. Gu, C. Liu and Z. Guo, J. Biol. Chem. **288** (26), 18673-18683 (2013).
- 85. A. J. Rice, A. Harrison, F. J. D. Alvarez, A. L. Davidson and H. W. Pinkett, J. Biol. Chem. **289** (21), 15005-15013 (2014).
- 86. P. Borbat and J. Freed, in *Structural Information from Spin-Labels and Intrinsic*Paramagnetic Centers in the Biosciences. Structure and Bonding., edited by J. Harmer and C.

  Timmel (Springer, Heidelberg, Germany, New York, USA, 2014), Vol. 152, pp. 1-82.
- 87. G. Jeschke, Ann. Rev. Phys. Chem. **63** (1), 419-446 (2012).
- 88. O. Schiemann and T. F. Prisner, Quart. Rev. Biophys. 40 (01), 1-53

- M53 10.1017/S003358350700460X (2007).
- 89. S. Dalapati, M. Addicoat, S. Jin, T. Sakurai, J. Gao, H. Xu, S. Irle, S. Seki and D. Jiang, Nat. Commun. **6** (1), 7786 (2015).
- 90. C. S. Diercks, M. J. Kalmutzki and O. M. Yaghi, Molecules **22**, 1575 doi: 10.3390/molecules22091575 (2017).
- 91. Q. Sun, B. Aguila, P. C. Lan and S. Ma, Adv. Mater. **31** (19), 1900008 (2019).
- 92. Q. Sun, C.-W. Fu, B. Aguila, J. Perman, S. Wang, H.-Y. Huang, F.-S. Xiao and S. Ma, J. Am. Chem. Soc. **140** (3), 984-992 (2018).
- 93. H.-X. Zhou, G. n. Rivas and A. P. Minton, Ann. Rev. Biophys. **37** (1), 375-397 (2008).
- 94. N. Pfanner and A. Geissler, Nat. Rev. Mol. Cell Biol. 2 (5), 339-349 (2001).
- 95. N. Pfanner, B. Warscheid and N. Wiedemann, Nat. Rev. Mol. Cell Biol. **20** (5), 267-284 (2019).
- 96. P. Dolezal, V. Likic, J. Tachezy and T. Lithgow, Science **313** (5785), 314-318 (2006).
- 97. T. A. Rapoport, L. Li and E. Park, Ann. Rev. Cell Dev. Biol. **33** (1), 369-390 (2017).
- 98. L. Ascherl, T. Sick, J. T. Margraf, S. H. Lapidus, M. Calik, C. Hettstedt, K. Karaghiosoff, M. Döblinger, T. Clark, K. W. Chapman, F. Auras and T. Bein, Nat. Chem. **8**, 310-316 (2016).
- 99. P. Li, S.-Y. Moon, M. A. Guelta, S. P. Harvey, J. T. Hupp and O. K. Farha, J. Am. Chem. Soc. **138** (26), 8052-8055 (2016).
- 100. F. Lyu, Y. Zhang, R. N. Zare, J. Ge and Z. Liu, Nano Lett. **14** (10), 5761-5765 (2014).
- 101. W. Liang, P. Wied, F. Carraro, C. J. Sumby, B. Nidetzky, C.-K. Tsung, P. Falcaro and C. J. Doonan, Chem. Rev. 121 (3), 1077-1129 (2021).
- 102. C. Doonan, R. Riccò, K. Liang, D. Bradshaw and P. Falcaro, Acc. Chem. Res. **50** (6), 1423-1432 (2017).

- 103. K. Liang, R. Ricco, C. M. Doherty, M. J. Styles, S. Bell, N. Kirby, S. Mudie, D. Haylock, A. J. Hill, C. J. Doonan and P. Falcaro, Nat. Commun. 6, 7240 (2015).
- 104. H. An, J. Song, T. Wang, N. Xiao, Z. Zhang, P. Cheng, H. Huang, S. Ma and Y. Chen, Angew. Chem. Int. Ed. 59 (10.1002/anie.202007827), 16764-16769 (2020).
- 105. D. E. Koshland, Proc. Natl Acad. Sci. 44 (2), 98-104 (1958).
- 106. E. Fischer, Berichte der deutschen chemischen Gesellschaft 27 (3), 2985-2993 (1894).
- 107. M. F. Perutz, M. G. Rossmann, A. F. Cullis, H. Muirhead, G. Will and A. North, Nature **185** (4711), 416-422 (1960).
- 108. J. C. Kendrew, G. Bodo, H. M. Dintzis, R. G. Parrish, H. Wyckoff and D. C. Phillips, Nature **181** (4610), 662-666 (1958).
- 109. R. H. Austin, K. Beeson, L. Eisenstein, H. Frauenfelder and I. Gunsalus, Biochemistry **14** (24), 5355-5373 (1975).
- 110. H. Frauenfelder, Proc. Natl Acad. Sci. 99 (suppl 1), 2479-2480 (2002).
- 111. E. T. Powers, R. I. Morimoto, A. Dillin, J. W. Kelly and W. E. Balch, Ann. Rev. Biochem. **78** (1), 959-991 (2009).
- 112. H. Neurath and K. A. Walsh, Proc. Natl. Acad. Sci. 73 (11), 3825-3832 (1976).
- 113. B. Turk, Nat. Rev. Drug Discov. **5** (9), 785-799 (2006).
- 114. P. Gurumallesh, K. Alagu, B. Ramakrishnan and S. Muthusamy, Int. J. Biol. Macromol. 128, 254-267 (2019).
- 115. M. Drag and G. S. Salvesen, Nat. Rev. Drug Discov. 9 (9), 690-701 (2010).
- 116. G. M. Su, I. A. Cordova, M. A. Brady, D. Prendergast and C. Wang, Polymer **99**, 782-796 (2016).
- 117. J. S. Higgins, Ann. Rev. Chem. Biomol. Eng. 7 (1), 1-28 (2016).

- 118. M. R. Hansen, R. Graf and H. W. Spiess, Acc. Chem. Res. 46 (9), 1996-2007 (2012).
- 119. J. Duhamel, Acc. Chem. Res. **39** (12), 953-960 (2006).
- 120. I. Hevus, A. Kohut and A. Voronov, Macromolecules 43 (18), 7488-7494 (2010).
- 121. A. Kohut, X. Dai, D. Pinnick, D. L. Schulz and A. Voronov, Soft Matt. 7 (8), 3717-3720 (2011).
- 122. I. Hevus, A. Modgil, J. Daniels, A. Kohut, C. Sun, S. Stafslien and A. Voronov, Biomacromolecules **13** (8), 2537-2545 (2012).
- 123. A. Kohut, O. Zholobko, I. Hevus and A. Voronov, Macromol. Chem. Phys. **218** (21), 1700344 (2017).
- 124. O. Boutureira and G. J. L. Bernardes, Chem. Rev. 115 (5), 2174-2195 (2015).
- 125. J. Kopeček, Adv. Drug Deliv. Rev. **65** (1), 49-59 (2013).
- 126. J. Yu, B. Panganiban and T. Xu, Ann. Rev. Phys. Chem. **64** (1), 631-657 (2013).
- 127. Y. Liu, J. Lee, K. M. Mansfield, J. H. Ko, S. Sallam, C. Wesdemiotis and H. D. Maynard, Bioconjug. Chem. **28** (3), 836-845 (2017).
- 128. A. P. Chapman, Adv. Drug Deliv. Rev. **54** (4), 531-545 (2002).